Evaluating Piezoelectric Materials and Vibration Modes for Power Conversion

Jessica D. Boles *Student Member, IEEE*, Joseph E. Bonavia, Pedro L. Acosta,
Yogesh K. Ramadass *Member, IEEE*, Jeffrey H. Lang *Fellow, IEEE* and David J. Perreault *Fellow, IEEE*

Abstract—Piezoelectric components offer several potential advantages to power conversion including high power density and efficiency capabilities compared to magnetics at small scales. Converter architectures have been developed for efficient utilization of piezoelectrics, but without fundamental criteria for designing the piezoelectric components themselves. In this paper, we derive figures of merit for the achievable efficiencies and power handling densities of piezoelectric materials and vibration modes based on realistic utilization in a power converter. These figures of merit are likewise accompanied by geometry conditions that serve as guidelines for high-efficiency, high-power-density piezoelectric resonator design. We demonstrate use of these metrics to evaluate commercially-available PZT and lithium niobate materials across seven vibration modes, and we validate the figures of merit and geometry conditions with numerical solutions of converter operation and experimental results. The proposed figures of merit are concluded to be highly representative metrics for the capabilities of piezoelectrics in power conversion, and these capabilities are shown to have favorable scaling properties for converter miniaturization.

Index Terms—piezoelectric resonators, piezoelectric materials, PZT, lithium niobate, dc-dc power conversion

TABLE I
MATERIAL STATE DEFINITIONS

u	Mechanical Displacement (m)
T	Mechanical Stress (N/m^2)
S	Mechanical Strain
E	Electric Field Strength (N/m)
D	Electric Flux Density (C/m^2)

TABLE II
MATERIAL PROPERTY DEFINITIONS

Q_m	Mechanical Quality Factor
k	Electromechanical Coupling Factor
v_a	Acoustic Velocity (m/s)
ρ	Mass Density (kg/m^3)
ε	Dielectric Constant (F/m)
s	Compliance Constant (m^2/N)
d	Piezoelectric Charge Constant (C/N)
c	Elastic Modulus (N/m^2)
e	Piezoelectric Strain Modulus (C/m^2)
σ	Poisson's Ratio
T_{max}	Maximum Mechanical Stress (N/m^2)
S_{max}	Maximum Mechanical Strain
E_{max}	Max. Electric Field Strength (N/m)

I. INTRODUCTION

Magnetic energy storage elements such as inductors and transformers pose fundamental limits to miniaturization for power electronics; as magnetics scale to smaller sizes, their power density and efficiency capabilities inherently decrease [2], [3]. This motivates exploration of power conversion based on other energy storage technologies that may be more conducive to miniaturization. Piezoelectrics, which store energy in the mechanical compliance and inertia of a piezoelectric material, have very high power density and efficiency capabilities with improved scaling properties to small sizes compared to magnetics [4]. Piezoelectrics also offer the advantages of planar form factors, ease of batch fabrication, and the potential to use the energy storage element itself for electrical isolation.

The promise of power conversion based on only piezoelectric energy storage is evident in magnetic-less converter designs realized in [5]–[10] with single-port piezoelectric resonators (PRs) and in [11]–[18] with multi-port piezoelectric transformers (PTs). In [5], we enumerate practical PR-based converter implementations that achieve high efficiency through

strategic utilization of the PR's resonant cycle, resulting in experimental efficiencies exceeding 99%. Other PR-based converter implementations are demonstrated in [6]-[7], and [8] explores use of high-frequency lithium niobate PRs to achieve high power density. However, criteria for selecting piezoelectric materials and/or designing PRs themselves remain less clear in the context of power conversion. PT structures and design strategies have been investigated in [18]–[27], though these methods are not directly applicable to PRs. Piezoelectric material and loss mechanisms have been reviewed extensively in [28], though primarily in the context of actuation.

In this work, we present figures of merit (FOMs) for piezoelectric materials and vibration modes specifically for use as energy storage in power electronics. Focusing on PRs, we derive FOMs for achievable efficiency and power handling density, which are shown to depend on only material properties assuming a realistic converter control sequence. We demonstrate use of these FOMs to compare commercially-available materials and vibration modes, and we validate the FOMs with both numerical solutions and experimental results. In addition to material and vibration mode selection, these FOM derivations aid PR geometry design and elucidate fundamental power handling scaling properties for PRs in realistic converter implementations.

Since the initial publication of this work in [1], we note that [8] has likewise explored material selection and PR design with an additional focus on fabrication.
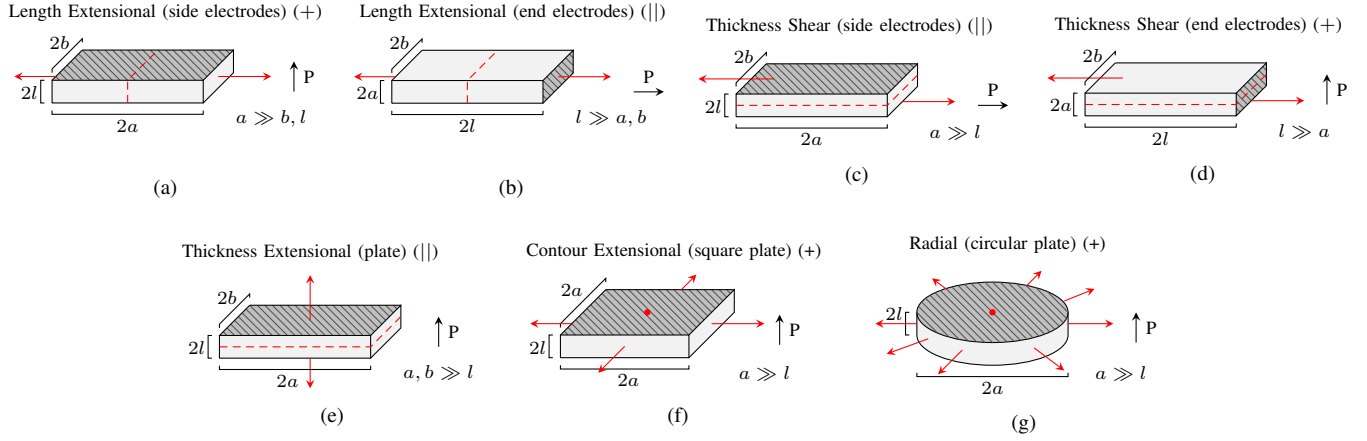
Fig. 1. Considered PR vibration modes with electrodes denoted by shaded areas, displacement direction(s) marked with red arrows, and nodes / nodal planes marked with red dots / dashed lines, respectively. The polarization direction of the PR is denoted with 'P', and each electrode is assumed to have area A with distance $2l$ between electrodes. All surfaces are assumed to have no externally-applied stress (i.e., all surfaces are traction-free), and the origin is assumed to be at the PR's center for analysis in Appendix A. For material property tensors, it should be noted that the "3" direction corresponds to the polarization axis.
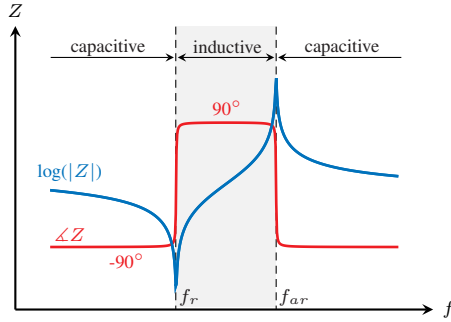

Fig. 2. PR impedance in the proximity of a vibration mode, where f_r is the resonant frequency and f_{ar} is the anti-resonant frequency.

TABLE III
PIEZOELECTRIC RESONATOR MODEL PARAMETERS [29]

Parameter	Parallel (‖)	Perpendicular (+)
G_f	$\frac{1}{l}$	$\frac{1}{a}$
γ_o	$\sqrt{\pi^2 - 8k^2}$	$\sqrt{\pi^2 + 8\frac{k^2}{1-k^2}}$
C_p	$\varepsilon^T(1-k^2)\frac{A}{2l}$	$\varepsilon^T(1-k^2)\frac{A}{2l}$
C	$\frac{8k^2}{\pi^2-8k^2}C_{p\|}$	$\frac{8k^2}{\pi^2(1-k^2)}C_{p+}$
L	$\frac{1}{2G_f^2k^2v_a^2C_{p\|}}$	$\frac{1-k^2}{2G_f^2k^2v_a^2C_{p+}}$
R	$\frac{1}{Q_m}\sqrt{\frac{L_\|}{C_\|}}$	$\frac{1}{Q_m}\sqrt{\frac{L_+}{C_+}}$

For thickness mode, $C_p = \varepsilon^S\frac{A}{2l}$. For radial mode parameters, see Appendix A(c).

II. PIEZOELECTRIC RESONATOR MODEL

PRs can be produced in a variety of shapes and electrode patterns, and each configuration has a unique set of compatible vibration modes depending the PR's polarization direction, electrode placement, and boundary conditions. To derive power-conversion-based metrics for piezoelectric materials, we focus on the fundamental frequencies of the vibration modes displayed in Fig. 1. These vibration modes can be grouped into two categories that permeate throughout this work: modes for which the applied and induced electric fields are parallel (‖), and modes for which these fields are perpendicular (+).

Piezoelectric materials are governed by coupled constitutive relations between mechanical strain (S), mechanical stress (T), electric field strength (E), and electric flux density (D) due to the direct and converse piezoelectric effects [29], [30]:

$$\mathbf{S} = \mathbf{s}^E\mathbf{T} + \mathbf{d}^t\mathbf{E} \tag{1}$$

$$\mathbf{D} = \mathbf{d}\mathbf{T} + \boldsymbol{\varepsilon}^T\mathbf{E} \tag{2}$$

in which bold quantities represent tensors. Parameters for these equations are defined in Tables I and II. Superscripts of S, T, E, or D indicate the respective state held constant during measurement (e.g., $\mathbf{s}^E$ indicates compliance at a zero or constant electric field), and t refers to the transpose.

Combined with the Newtonian equation of motion, (1) and (2) reduce to an acoustic wave equation that dictates sinusoidal time- and space-dependent solutions for u, S, T, and E; this is described with more detail in Appendix A. With all surfaces in Fig. 1 assumed to be traction-free, the maximum amplitudes of S, T, and E each occur at the center of the PR.

The frequency f of the acoustic wave propagating through the PR is expressed as

$$f = \frac{\kappa}{2\pi}v_a = G_f\frac{\kappa_o}{2\pi}v_a \tag{3}$$

in which κ is the wave number (in rad/m) and v_a is the acoustic velocity (in m/s) of the PR material [29]. We also define κ_o to be the geometry-normalized wave number (in rad), from which we have extracted the geometry-dependent factor G_f. G_f is different for parallel and perpendicular vibration modes and is displayed for each in Table III. For a given material, G_f sets the resonant frequency of a PR design.

The PR's electrical impedance can be likewise derived from the acoustic wave solution and is shown in Fig. 2 as a function of f. The PR exhibits inductive behavior in the region between the resonant (f_r) and anti-resonant (f_{ar}) frequencies; this region is of most interest to power conversion since inductive loading enables zero voltage switching (ZVS) and
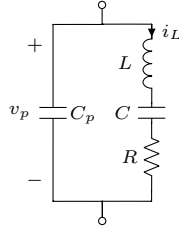
Fig. 3. Butterworth-Van Dyke circuit model for PRs [31]. Parameters are defined in Table III [29].

Fig. 4. Example topology for the V_{in}-V_{out}, *Zero*, V_{out} switching sequence proposed in [5].

Fig. 5. Experimental waveforms and associated switch signals for switching sequence V_{in}-V_{out}, *Zero*, V_{out} from [5]. Numbers 1-6B designate connected/zero stages (odd) and open stages (even). V_{in} = 100 V, V_{out} = 60 V, P_{out} = 4 W.

other high-efficiency behaviors [5]. The inductive region spans the following ranges of κ_o for parallel ($\|$) and perpendicular ($+$) vibration modes, respectively:

$$\frac{\gamma_{o\|}}{2} < \kappa_{o\|} < \frac{\pi}{2} \tag{4}$$

$$\frac{\pi}{2} < \kappa_{o+} < \frac{\gamma_{o+}}{2} \tag{5}$$

for which factor γ_o is displayed in Table III.

The PR impedance characteristic shown in Fig. 2 can be modeled by an equivalent electrical circuit (ie. the Butterworth-Van Dyke model [31]) illustrated in Fig. 3. For excitation of a PR's fundamental frequency, this model has the parameters shown in Table III, which are generalized to parallel and perpendicular vibration modes [29], [32], [33]. A is the electrode area, $2l$ is the distance between the electrodes, and the material parameters of interest are shown for each vibration mode in Appendix A. This electrical model serves as the basis for how we conceptualize the PR's behavior: f_r corresponds to series resonance between L and C, and f_{ar} occurs at parallel resonance between C_p and the series combination of L and C. The model's full derivation for all considered modes can be found in [29], and [1] provides this derivation among others for the length extensional mode[1].

III. AMPLITUDE OF RESONANCE MODEL

We employ the circuit model of Section II to analyze the PR's behavior in a power converter. Because PRs tend to have very high quality factors in the proximity of their resonant frequencies, we assume i_L to be sinusoidal. The amplitude of i_L (I_L) then provides insight into the amplitude of the PR's mechanical resonance, which dictates its mechanical energy storage and loss [5].

A. Assumed Converter Operation

To model PR behavior as utilized in a converter, we assume operation based on either of the highest-efficiency step-down switching sequences analyzed in [5]. These sequences are each comprised of six stages: three "connected/zero stages" (ie. stages in which the PR is connected to the source-load system) alternated with three "open stages" (stages in which the PR is open-circuited and C_p charges/discharges through

[1]The vibration mode analyzed in [1] is referred to as the thickness extensional mode, though it assumes the k_{33} coupling coefficient. Thus, the analysis in [1] corresponds to this work's length extensional mode (with end electrodes) analysis, except with one electrode rigidly mounted.
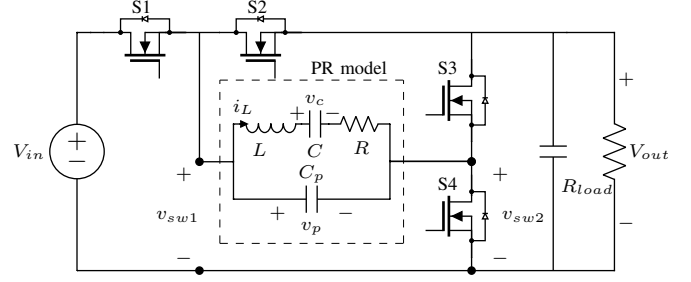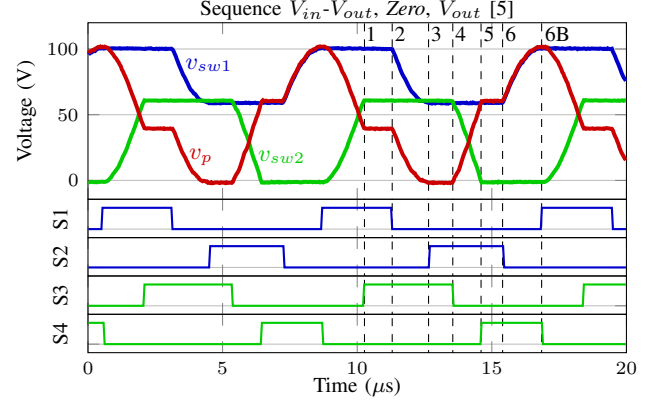
resonance). Further, these switching sequences are constrained for the following high-efficiency behaviors:

1) Resonant "soft" charging/discharging of the PR's C_p during open stages.
2) Zero-voltage switching (ZVS) of all switches.
3) All-positive instantaneous power transfer during connected stages.

These highest-efficiency switching sequences are capable of constant-efficiency voltage regulation for $\frac{1}{2} \leq \frac{V_{out}}{V_{in}} \leq 1$. One such switching sequence is referred to as V_{in}-V_{out}, *Zero*, V_{out}, named according to its connected/zero stage voltages [5]. An example topology for realizing this sequence is visualized in Fig. 4 with corresponding waveforms in Fig. 5; we utilize this implementation for experimental validation in Section VII(b).

B. Model Introduction

The PR's ideal amplitude of resonance (I_L) can be calculated from the total magnitude of charge transferred by i_L during each resonant cycle (q_{total}) as illustrated in Fig. 6. This charge transfer calculation depends on the converter's specific switching sequence and considers both connected/zero stages and open stages for realistic representation [5]. The highest-efficiency sequences discussed in Section III(a) have the following I_L, which varies based on operating point:

$$I_L := \frac{\pi}{2} f q_{total} = \pi \left(\frac{P_{out}}{V_{in}} + f C_p V_{in} \right) \tag{6}$$

where $P_{out} = \frac{V_{out}^2}{R_{load}}$ as defined in Fig. 4.

TABLE IV
MAXIMUM AMPLITUDES OF RESONANCE BASED ON MATERIAL LIMITS

Vibration Mode	I_{LmaxSo}	I_{LmaxTo}	I_{LmaxEo}	I_{LmaxLo}
Length Extensional (s)	$v_a \dfrac{d_{31}}{s_{11}^E} S_{max}\sin(\kappa_o)$	$v_a d_{31} T_{max}\cot(\tfrac{\kappa_o}{2})$	$v_a k_{31}^2 \varepsilon_{33}^T E_{max}\tan(\kappa_o)$	$\sqrt{\dfrac{4 Q_m k_{31}^2 \varepsilon_{33}^T v_a}{\pi}}\, H$
Length Extensional (e)	$v_a \dfrac{d_{33}}{s_{33}^E} S_{max}\sin(\kappa_o)$	$v_a d_{33}(1-k_{33}^2) T_{max}\cot(\tfrac{\kappa_o}{2})$	$v_a k_{33}^2 \varepsilon_{33}^S E_{max}\dfrac{\sin(\kappa_o)}{\cos(\kappa_o)-k_{33}^2}$	$\sqrt{\dfrac{4 Q_m k_{33}^2 \varepsilon_{33}^S v_a}{\gamma_o}}\, H$
Thickness Shear (side)	$v_a \dfrac{d_{15}}{s_{55}^E} S_{max}\sin(\kappa_o)$	$v_a d_{15}(1-k_{15}^2) T_{max}\cot(\tfrac{\kappa_o}{2})$	$v_a k_{15}^2 \varepsilon_{11}^S E_{max}\dfrac{\sin(\kappa_o)}{\cos(\kappa_o)-k_{15}^2}$	$\sqrt{\dfrac{4 Q_m k_{15}^2 \varepsilon_{11}^S v_a}{\gamma_o}}\, H$
Thickness Shear (end)	$v_a \dfrac{d_{15}}{s_{55}^E} S_{max}\sin(\kappa_o)$	$v_a d_{15} T_{max}\cot(\tfrac{\kappa_o}{2})$	$v_a k_{15}^2 \varepsilon_{11}^T E_{max}\tan(\kappa_o)$	$\sqrt{\dfrac{4 Q_m k_{15}^2 \varepsilon_{11}^T v_a}{\pi}}\, H$
Thickness Extensional	$v_a e_{33} S_{max}\sin(\kappa_o)$	$v_a \dfrac{e_{33}(1-k_t^2)}{c_{33}^E} T_{max}\cot(\tfrac{\kappa_o}{2})$	$v_a k_t^2 \varepsilon_{33}^S E_{max}\dfrac{\sin(\kappa_o)}{\cos(\kappa_o)-k_t^2}$	$\sqrt{\dfrac{4 Q_m k_t^2 \varepsilon_{33}^S v_a}{\gamma_o}}\, H$
Contour Extensional	$\dfrac{2 d_{31} v_a}{s_{11}^E(1-\sigma)} S_{max}\sin(\kappa_o)$	$2 v_a d_{31} T_{max}\cot(\tfrac{\kappa_o}{2})$	$v_a k_p^2 \varepsilon_{33}^T E_{max}\tan(\kappa_o)$	$\sqrt{\dfrac{4 Q_m k_p^2 \varepsilon_{33}^T v_a}{\pi}}\, H$
Radial	$\dfrac{4 d_{31} v_a}{s_{11}^E(1-\sigma)} S_{max} J_1(\kappa_o)$	$\dfrac{2 v_a d_{31}(1+\sigma)}{\frac{1}{2}(1+\sigma)-\Psi} T_{max} J_1(\kappa_o)$	$v_a k_p^2 \varepsilon_{33}^T(1+\sigma) E_{max}\dfrac{J_1(\kappa_o)}{\Psi}$	$\sqrt{\dfrac{2 Q_m k_p^2 \varepsilon_{33}^T v_a}{\frac{\kappa_{o,r}}{1+\sigma}-\frac{1-\sigma}{\kappa_{o,r}}}}\, H$

Numerical subscripts indicate the tensor components relevant for each mode [29]. For I_{LmaxLo}, we have substituted $H = \left(\frac{P_{loss}}{A_s}\right)_{max}$.
For radial mode, Appendix A(c) contains the definition for Ψ and series expansions for Bessel functions.
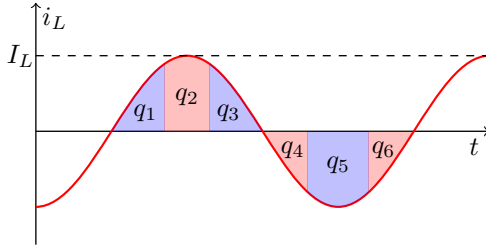

Fig. 6. Sinusoidal approximation of i_L and resulting amplitude of resonance I_L, based on the charge transfer q_n required of each switching stage n [5].

In accordance with the switching sequences discussed in Section III(a), this I_L equation assumes soft charging/discharging of the PR's C_p, ZVS of all switches, and all-positive instantaneous power transfer for high efficiency [5]. Thus, (6) models the PR's amplitude of resonance for typical converter operation, which we assume throughout this work.

C. Material Limits

A PR's maximum amplitude of resonance (I_{Lmax}) may be determined by its material's limits for strain (S_{max}), stress (T_{max}), and electric field (E_{max}). Such potential limits include yield stress and strain, as well as coercive field (i.e., the electric field strength at which depolarization occurs). We can derive the relationship between I_L and the PR's physical states using the constitutive relations (1)-(2) and the equation of motion. This results in the following relationship between I_L and the amplitude of mechanical displacement (Δ) as derived in Appendix B:

$$I_L = \kappa A G_f \frac{v_a d}{s^E} \Delta \sin(\kappa_o) \qquad (7)$$

Then, S, T and E can each be related to I_L through Δ. This strategy can be utilized to determine the I_L limits corresponding to maximum strain (I_{LmaxS}), maximum stress (I_{LmaxT}), and maximum E field (I_{LmaxE}) as demonstrated in Appendix B. It is shown that I_{LmaxS}, I_{LmaxT}, and I_{LmaxE} have identical geometry terms, so their geometry-normalized

values (referred to as I_{LmaxSo}, I_{LmaxTo} and I_{LmaxEo}, respectively) are summarized for each considered vibration mode in Table IV. The lowest-magnitude limit can be considered the geometry-normalized maximum for I_L:

$$I_{Lmaxo} := \frac{I_{Lmax}}{A G_f} = \min(I_{LmaxSo}, I_{LmaxTo}, I_{LmaxEo}) \qquad (8)$$

Thus, the geometry-normalized limit I_{Lmaxo} (and which physical limit constrains it) can be determined based on only material parameters and limits. I_{Lmaxo} is employed to determine maximum power handling density in Section V.

D. Areal Loss Density Limit

Thermal management limitations may confine a PR's amplitude of resonance to lower bounds than its material's physical limits, so we likewise derive an I_L limit based on areal loss density. Material-dependent losses in the PR include mechanical loss and dielectric loss; since mechanical loss tends to dominate close to resonance [34], we focus on only mechanical loss in the context of this work. We estimate mechanical loss using I_L and R [5]:

$$P_{loss} := \frac{1}{2} I_L^2 R \qquad (9)$$

For an I_L limit based on areal loss density, we assume that most PR heat extraction occurs through a surface with area A_s, and that a thermal design can safely accommodate a certain quantity of PR loss per A_s. This areal loss density relates to the PR's operation as follows:

$$\frac{P_{loss}}{A_s} = \frac{1}{2}\frac{I_L^2 R}{A_s} = \frac{1}{2} I_{Lo}^2 R_o \qquad (10)$$

in which we have extracted geometry parameters from I_L and R, assuming $A_s = A$ for parallel ($\|$) modes, $A_s = G_f A l$ for perpendicular ($+$) modes as defined in Table VI, and R_o for all modes as defined in Table V (where $R_o = GR$, in which G contains all geometry terms). For these assumed surfaces, all geometry terms cancel and (10) shows a direct relationship between areal loss density and I_{Lo}. This equation can be rearranged to define a loss-limited maximum for I_{Lo}:

Vibration Mode	G	B_o	R_o	FOM$_M$	γ_o
Length Extensional (s)	$\dfrac{4b}{l}$	$\varepsilon_{33}^T(1-k_{31}^2)\dfrac{\kappa_o v_a}{4\pi}$	$\dfrac{\pi}{2Q_m k_{31}^2 \varepsilon_{33}^T v_a}$	$4Q_m \dfrac{k_{31}^2}{1-k_{31}^2}\dfrac{1}{\pi^2 \bar{\kappa}_o}$	$\sqrt{\pi^2 + 8\dfrac{k_{31}^2}{1-k_{31}^2}}$
Length Extensional (e)	$\dfrac{A}{l^2}$	$\varepsilon_{33}^T(1-k_{33}^2)\dfrac{\kappa_o v_a}{4\pi}$	$\dfrac{\gamma_o}{2Q_m k_{33}^2 \varepsilon_{33}^T(1-k_{33}^2)v_a}$	$4Q_m k_{33}^2 \dfrac{1}{\pi\gamma_o \bar{\kappa}_o}$	$\sqrt{\pi^2 - 8k_{33}^2}$
Thickness Shear (side)	$\dfrac{A}{l^2}$	$\varepsilon_{11}^S \dfrac{\kappa_o v_a}{4\pi}$	$\dfrac{\gamma_o}{2Q_m k_{15}^2 \varepsilon_{11}^S v_a}$	$4Q_m k_{15}^2 \dfrac{1}{\pi\gamma_o \bar{\kappa}_o}$	$\sqrt{\pi^2 - 8k_{15}^2}$
Thickness Shear (end)	$\dfrac{4b}{l}$	$\varepsilon_{11}^S \dfrac{\kappa_o v_a}{4\pi}$	$\dfrac{\pi}{2Q_m k_{15}^2 \varepsilon_{11}^T v_a}$	$4Q_m \dfrac{k_{15}^2}{1-k_{15}^2}\dfrac{1}{\pi^2 \bar{\kappa}_o}$	$\sqrt{\pi^2 + 8\dfrac{k_{15}^2}{1-k_{15}^2}}$
Thickness Extensional	$\dfrac{A}{l^2}$	$\varepsilon_{33}^S \dfrac{\kappa_o v_a}{4\pi}$	$\dfrac{\gamma_o}{2Q_m k_t^2 \varepsilon_{33}^S v_a}$	$4Q_m k_t^2 \dfrac{1}{\pi\gamma_o \bar{\kappa}_o}$	$\sqrt{\pi^2 - 8k_t^2}$
Contour Extensional	$\dfrac{4a}{l}$	$\varepsilon_{33}^T(1-k_p^2)\dfrac{\kappa_o v_a}{4\pi}$	$\dfrac{\pi}{2Q_m k_p^2 \varepsilon_{33}^T v_a}$	$4Q_m \dfrac{k_p^2}{1-k_p^2}\dfrac{1}{\pi^2 \bar{\kappa}_o}$	$\sqrt{\pi^2 + 8\dfrac{k_p^2}{1-k_p^2}}$
Radial	$\dfrac{\pi a}{l}$	$\varepsilon_{33}^T(1-k_p^2)\dfrac{\kappa_o v_a}{4\pi}$	$\dfrac{\kappa_{o,r}^2-(1-\sigma^2)}{Q_m \kappa_{o,r}(1+\sigma)k_p^2 \varepsilon_{33}^T v_a}$	$Q_m \dfrac{k_p^2}{1-k_p^2}\dfrac{2}{\pi\bar{\kappa}_o}\dfrac{\kappa_{o,r}(1+\sigma)}{\kappa_{o,r}^2-(1-\sigma^2)}$	Appendix A(c)

Numerical subscripts indicate the tensor components relevant for each mode [29]. From (21), $\bar{\kappa}_o = \frac{\pi\gamma_o}{\pi+\gamma_o}$ (see Appendix A(c) for radial mode).

$$I_{LmaxLo} = \sqrt{\frac{2}{R_o}\left(\frac{P_{loss}}{A_s}\right)_{max}} \qquad (11)$$

For perpendicular modes in which both non-l dimensions are equal, an areal loss density based on A can be scaled to A_s using $\frac{P_{loss}}{A_s} = \frac{\widehat{G}}{4}\frac{P_{loss}}{A}$ (for contour extensional mode) or $\frac{\widehat{G}}{\pi}\frac{P_{loss}}{A}$ (for radial mode). This assumes a PR design will adhere to $\widehat{G}$, the condition for G corresponding to maximum efficiency as derived in Section IV(a).

I_{LmaxLo} is displayed in Table IV for each mode and can be directly compared to I_{LmaxSo}, I_{LmaxTo} and I_{LmaxEo} in (8) to determine I_{Lmaxo}. It can also be utilized in Section V to calculate loss-limited energy and power handling densities.

IV. MECHANICAL EFFICIENCY FIGURE OF MERIT

To quantitatively compare piezoelectric materials and vibration modes for power conversion, we first focus on achievable PR efficiency; this has implications for both operating cost and thermal management. Efficiency can be expressed as

$$\eta := \frac{P_{out}}{P_{out} + P_{loss}} = \frac{1}{1 + \frac{P_{loss}}{P_{out}}} \qquad (12)$$

Thus, the impact of piezoelectric material properties on efficiency can be examined through *loss ratio* P_{loss}/P_{out}, which is desired to be as low as possible. As discussed in Section III, we focus on only mechanical loss for this FOM.

A. Minimum Mechanical Loss Ratio

The mechanical loss ratio of a PR can be expressed as follows, assuming P_{loss} in (9) and I_L in (6):

$$\frac{P_{loss}}{P_{out}} = \frac{\frac{1}{2}I_L^2 R}{P_{out}} = \frac{\pi^2}{2}\left(\frac{P_{out}}{V_{in}^2}R + 2BR + \frac{V_{in}^2 B^2}{P_{out}}R\right) \qquad (13)$$

in which we have substituted

$$B := fC_p \qquad (14)$$

This loss ratio equation has only two operating point parameters (V_{in} and P_{out}) and two PR-dependent parameters (B and R). We can explicitly separate the PR's material and geometry properties by extracting all geometry parameters from B and R, which have the same lumped geometry term G (as reciprocals), leaving only the material-dependent B_o and R_o, respectively. Thus, (13) can be rewritten as

$$\frac{P_{loss}}{P_{out}} = \frac{\pi^2}{2}\left(\frac{P_{out}}{V_{in}^2}\frac{R_o}{G} + 2B_o R_o + \frac{V_{in}^2}{P_{out}}GB_o^2 R_o\right) \qquad (15)$$

where

$$G := G_f \frac{A}{l} = \frac{B}{B_o} = \frac{R_o}{R} \qquad (16)$$

These parameters are displayed for each vibration mode in Table V. It should be noted that we treat Q_m as a material property provided by the manufacturer for the purposes of this study, though Q_m may realistically vary from this value based on PR shape, vibration mode, and mounting structure.

To derive the minimum mechanical loss ratio, we assume that the designer has the flexibility to choose the PR's geometric dimensions. The loss ratio equation reached in (15) is a second-order equation with respect to G as illustrated in Fig. 7(a). Minimizing (15) with respect to G reveals the following G condition (denoted by $\widehat{G}$) and corresponding minimum mechanical loss ratio:

$$\widehat{G} = \frac{P_{out}}{V_{in}^2 B_o} = \frac{V_{out}^2}{V_{in}^2 B_o R_{load}} \qquad (17)$$

$$\Rightarrow \quad \left(\frac{P_{loss}}{P_{out}}\right)_{min} = 2\pi^2 B_o R_o \qquad (18)$$

The condition in (17) cancels the operating point, load, and PR geometry parameters in the loss ratio equation (18), so *the minimum achievable mechanical loss ratio for a PR depends on only its material properties* (i.e., quantities assumed in Table II). Taking the inverse of (18), the following unitless factor can be therefore considered a mechanical efficiency FOM (FOM$_M$) for PR materials and vibration modes:

$$\text{FOM}_M := \frac{1}{2\pi^2 B_o R_o} \qquad (19)$$

FOM$_M$ is desired to be as large as possible, and it is summarized in Table V for the considered vibration modes. For an example of this derivation for a single mode, see [1].

B. Geometry Condition

A PR can be designed to achieve its material's minimum mechanical loss ratio at a nominal operating point by satisfying $G = \widehat{G}$ with its geometric dimensions. The order of magnitude of B_o ranges from 10^{-8} to 10^{-6} for most piezoelectric materials, which requires $\widehat{G} >> 1$ in (17) for most power conversion applications. Thus, $\widehat{G}$ often dictates l to be the shortest geometric dimension, resulting in primarily planar PR designs. Parallel vibration modes can be particularly advantageous for satisfying large $\widehat{G}$ values in that both the numerator (A) and denominator (l^2) have squared length dimensions. Mode configurations for which l is not the shortest dimension (length extensional and thickness shear, each with end electrodes) have limited practicality; their relative dimension assumptions can only be maintained for very high $\frac{V_{in}^2}{P_{out}}$.

C. Operating Frequency

Though B_o and R_o have no geometry dependence, B_o depends on κ_o, which spans the ranges of (4) and (5) for the inductive region shown in Fig. 2. Although the switching sequence described in Section III(a) naturally spans this inductive region, frequency is *not* an independent control variable. To maintain the high-efficiency behaviors described in Section III, the exact operating frequency (and therefore exact κ_o) is dictated by the operating point [5].

Thus, we determine the frequency and κ_o that correspond to the minimum loss ratio operating point in (17)-(18) for use in the FOMs of Sections IV and V (though this is also useful for broader converter design). Inserting $\widehat{G}$ into (6) reveals both addends of I_L to be equal for this condition, which implies that the PR's charge transfer is split evenly between connected/zero stages (resonating at f_r with period $\frac{1}{f_r}$) and open stages (resonating at f_{ar} with period $\frac{1}{f_{ar}}$). Thus, both stage types require half of their respective periods (for each transferring $\frac{1}{2}Q_{total}$), so the total period adds to $\frac{1}{\bar{f}} = \frac{1}{2f_r} + \frac{1}{2f_{ar}}$. This reveals the highest-efficiency operating frequency to be the harmonic mean of f_r and f_{ar}:

$$\bar{f} := \frac{2 f_r f_{ar}}{f_r + f_{ar}} \qquad (20)$$

which has the following geometry-normalized wave number (also derived for radial mode in Appendix A(c)):

$$\bar{\kappa}_o := \frac{\pi \gamma_o}{\pi + \gamma_o} \qquad (21)$$

Thus, assuming the switching sequence constraints listed in Section III(a) are met, this is the operating frequency for which (17) is satisfied and the minimum loss ratio occurs. This is the operating frequency assumed for the remainder of this work.

V. POWER DENSITY FIGURES OF MERIT

A second point of comparison for piezoelectric materials and vibration modes is achievable power handling density, which poses a boundary for converter miniaturization. Useful power density metrics must consider how the PR is to be utilized in a converter (ie. not just energy storage capability), so we again assume the amplitude of resonance model in
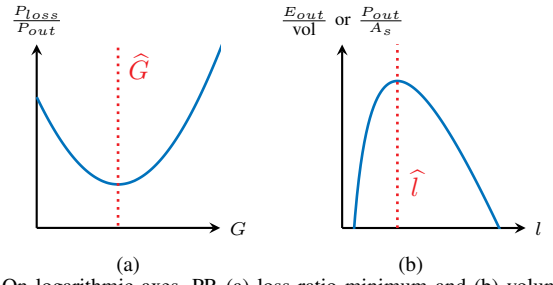

Fig. 7. On logarithmic axes, PR (a) loss ratio minimum and (b) volumetric energy handling density (or areal power handling density) maximum.

Section III. To model the PR's power handling capability as a function of operating constraints, (6) can be rearranged such that power delivered to the load is the following function of I_L:

$$P_{out} = \frac{1}{\pi} V_{in} I_L - C_p f V_{in}^2 = \frac{1}{\pi} V_{in} I_L - B V_{in}^2 \qquad (22)$$

With (22), we derive maximum energy and power handling densities considering the physical and loss-density limits for I_L presented in Sections III(b) and III(c), respectively.

A. Volumetric Energy Handling Density

Volumetric power density is a common metric for converter power handling capability with respect to size. The PR's volumetric power density can be derived by first dividing (22) by volume, where $\text{vol} = 2Al$:

$$\frac{P_{out}}{\text{vol}} = \frac{P_{out}}{2Al} = G_f \Big(\frac{1}{2\pi l} V_{in} I_{Lmaxo} - \frac{1}{2l^2} B_o V_{in}^2 \Big) \qquad (23)$$

in which I_L has been set equal to I_{Lmax} and geometry terms have been separated from material properties.

It is evident that a PR's volumetric power density is directly proportional to G_f, and therefore f. The operating frequency of a converter determines its driving and control requirements, so we elect to normalize (23) to f for even comparison between PR vibration modes with respect to converter capability. Such normalization results in the following expression for volumetric *energy handling* density, defined as the quantity of energy delivered to the load in one resonant cycle divided by volume (not to be confused with energy storage density):

$$\frac{E_{out}}{\text{vol}} = \frac{P_{out}}{\text{vol} \cdot f} = \frac{1}{\kappa_o v_a} \Big(\frac{1}{l} V_{in} I_{Lmaxo} - \frac{\pi}{l^2} B_o V_{in}^2 \Big) \qquad (24)$$

We can then maximize this expression by assuming the designer has the flexibility to choose l. Maximizing (24) with respect to l as illustrated in Fig. 7(b) results in the following l condition (denoted $\widehat{l}$) and maximum volumetric energy handling density:

$$\widehat{l} = 2\pi \frac{B_o V_{in}}{I_{Lmaxo}} \qquad (25)$$

$$\Rightarrow \quad \Big(\frac{E_{out}}{\text{vol}} \Big)_{max} = \frac{I_{Lmaxo}^2}{4\pi \kappa_o v_a B_o} \qquad (26)$$

Thus, all operating point and geometry terms cancel in (26), and the maximum volumetric energy handling density of a PR depends on only its material properties (defined in Table

Vibration Mode	FOM_{VED}	FOM_{APD}	A_s
Length Extensional (s)	$\dfrac{I_{Lmaxo}^2}{\bar\kappa_o^2 v_a^2 \varepsilon_{33}^T(1-k_{31}^2)}$	$\dfrac{I_{Lmaxo}^2}{\pi\bar\kappa_o \varepsilon_{33}^T(1-k_{31}^2)v_a}$	$4bl$
Length Extensional (e)	$\dfrac{I_{Lmaxo}^2}{\bar\kappa_o^2 v_a^2 \varepsilon_{33}^T(1-k_{33}^2)}$	$\dfrac{I_{Lmaxo}^2}{\pi\bar\kappa_o \varepsilon_{33}^T(1-k_{33}^2)v_a}$	A
Thickness Shear (side)	$\dfrac{I_{Lmaxo}^2}{\bar\kappa_o^2 v_a^2 \varepsilon_{11}^S}$	$\dfrac{I_{Lmaxo}^2}{\pi\bar\kappa_o \varepsilon_{11}^S v_a}$	A
Thickness Shear (end)	$\dfrac{I_{Lmaxo}^2}{\bar\kappa_o^2 v_a^2 \varepsilon_{11}^S}$	$\dfrac{I_{Lmaxo}^2}{\pi\bar\kappa_o \varepsilon_{11}^S v_a}$	$4bl$
Thickness Extensional	$\dfrac{I_{Lmaxo}^2}{\bar\kappa_o^2 v_a^2 \varepsilon_{33}^S}$	$\dfrac{I_{Lmaxo}^2}{\pi\bar\kappa_o \varepsilon_{33}^S v_a}$	A
Contour Extensional	$\dfrac{I_{Lmaxo}^2}{\bar\kappa_o^2 v_a^2 \varepsilon_{33}^T(1-k_p^2)}$	$\dfrac{I_{Lmaxo}^2}{\pi\bar\kappa_o \varepsilon_{33}^T(1-k_p^2)v_a}$	$4al$
Radial	$\dfrac{I_{Lmaxo}^2}{\bar\kappa_o^2 v_a^2 \varepsilon_{33}^T(1-k_p^2)}$	$\dfrac{I_{Lmaxo}^2}{\pi\bar\kappa_o \varepsilon_{33}^T(1-k_p^2)v_a}$	πal

Numerical subscripts indicate the tensor components relevant for each mode [29]. From (21), $\bar\kappa_o = \frac{\pi\gamma_o}{\pi+\gamma_o}$ (see Appendix A(c) for radial mode).

II). The following can therefore be considered a volumetric energy handling density FOM for direct comparison between PR materials and vibration modes:

$$\text{FOM}_{VED} := \frac{I_{Lmaxo}^2}{4\pi\kappa_o v_a B_o} \qquad (27)$$

which has units J/m³. FOM_{VED} is summarized for various PR vibration modes in Table VI; we suggest use of the minimum-loss wave number $\bar\kappa_o$ as detailed in Section IV(c). The corresponding volumetric power density can be calculated by multiplying FOM_{VED} by a desired operating frequency, though this frequency depends on $\hat{l}$ for parallel modes[2].

B. Areal Power Handling Density

In some applications, power handling capability per footprint area may be more useful to the designer than volumetric energy handling density. Areal power density also becomes more relevant for highly-planar PR designs, as often dictated by $\hat{G}$ in (17) for maximum efficiency. Like Section III(c), we assume the area of interest $A_s = A$ for parallel modes and $A_s = G_f Al$ for perpendicular modes as displayed in Table VI. Similar to (23), the areal power density can be written as follows with $I_L = I_{Lmax}$ and geometry terms extracted:

$$\frac{P_{out}}{A_s} = \frac{1}{\pi l}V_{in}I_{Lmaxo} - \frac{1}{l^2}B_o V_{in}^2 \qquad (28)$$

This expression can be likewise maximized with respect to l, resulting in the same $\hat{l}$ condition and the following maximum areal power density:

$$\hat{l} = \frac{2\pi B_o V_{in}}{I_{Lmaxo}} \qquad (29)$$

$$\Rightarrow \quad \left(\frac{P_{out}}{A_s}\right)_{max} = \frac{I_{Lmaxo}^2}{4\pi^2 B_o} \qquad (30)$$

[2]For parallel modes, maximum volumetric power density occurs for $l = \frac{3}{4}\hat{l}$, though with diminishing returns with respect to frequency for $l < \hat{l}$. The volumetric power density at $l = \frac{3}{4}\hat{l}$ is ≈ 18.5 % greater than that at $l = \hat{l}$.

Like the maximum volumetric energy handling density in (26), the maximum areal power density for a PR depends on only its material properties. Thus, (30) serves as an areal power handling density FOM for PR materials and vibration modes:

$$\text{FOM}_{APD\|} := \frac{I_{Lmaxo}^2}{4\pi^2 B_o} \qquad (31)$$

with units W/m². FOM_{APD} equals FOM_{VED} scaled by $\frac{\kappa_o v_a}{\pi}$ and is likewise summarized in Table VI for each considered vibration mode. It should be noted that FOM_{APD} assumes the area A_s corresponds to the PR's relevant footprint, though the validity of this assumption depends on the PR's shape, vibration mode, and mounting structure. For contour and radial modes (i.e. modes for which both non-l dimensions are equal), FOM_{APD} may be respectively scaled by $\frac{4}{\hat{G}}$ and $\frac{\pi}{\hat{G}}$ for representative areal power densities based on A, assuming a PR design will adhere to the $\hat{G}$ condition for maximum efficiency. Since $\hat{G}$ varies by operating point, this scaled FOM_{APD} for such configurations may introduce dependence on operating point information.

VI. MATERIAL AND VIBRATION MODE COMPARISON

Equipped with FOMs for mechanical efficiency and power density, we now demonstrate use of these FOMs to evaluate piezoelectric materials and vibration modes for power conversion. We first compare relative capabilities of commercially-available variants of hard PZT, the most widely-utilized piezoelectric material for sensing, actuation, transduction, and energy harvesting applications. This is followed by a comparison of the seven vibration modes discussed herein for PZT and lithium niobate (LiNbO$_3$), a second piezoelectric material of emerging interest for power conversion [4], [8]. It should be noted that the results of these studies are meant to be more demonstrative of the FOMs than prescriptive of the materials; the results are sensitive to variation between manufacturers in terms of measurement procedure and/or reporting of material properties (particularly for E_{max} and Q_m). This topic merits a detailed experimental characterization of such materials and vibration modes, which is beyond the scope of this work.

A. Comparing Materials

First, we compare commercial PZT materials based on efficiency and power density for the thickness extensional and thickness shear vibration modes (with side electrodes). We collect and/or calculate the following properties for 30 hard PZT materials from eight different manufacturers: Q_m, ε_{33}^S, ε_{11}^S, k_t, k_{15}, and v_a for each mode ($v_a = \frac{\pi N}{\kappa_{o,r}}$, where N is the manufacturer-provided frequency constant). Sinusoidal amplitude E_{max} is conservatively estimated to be 500 V/mm for all materials, and power density capability is assumed to be limited by this E_{max}.

We use these properties to calculate FOM_M and FOM_{APD} for both modes with each material. Fig. 8 displays these results with one FOM on each axis, and the considered materials exhibit wide variation in terms of capability. The thickness extensional mode (denoted by unfilled markers) generally
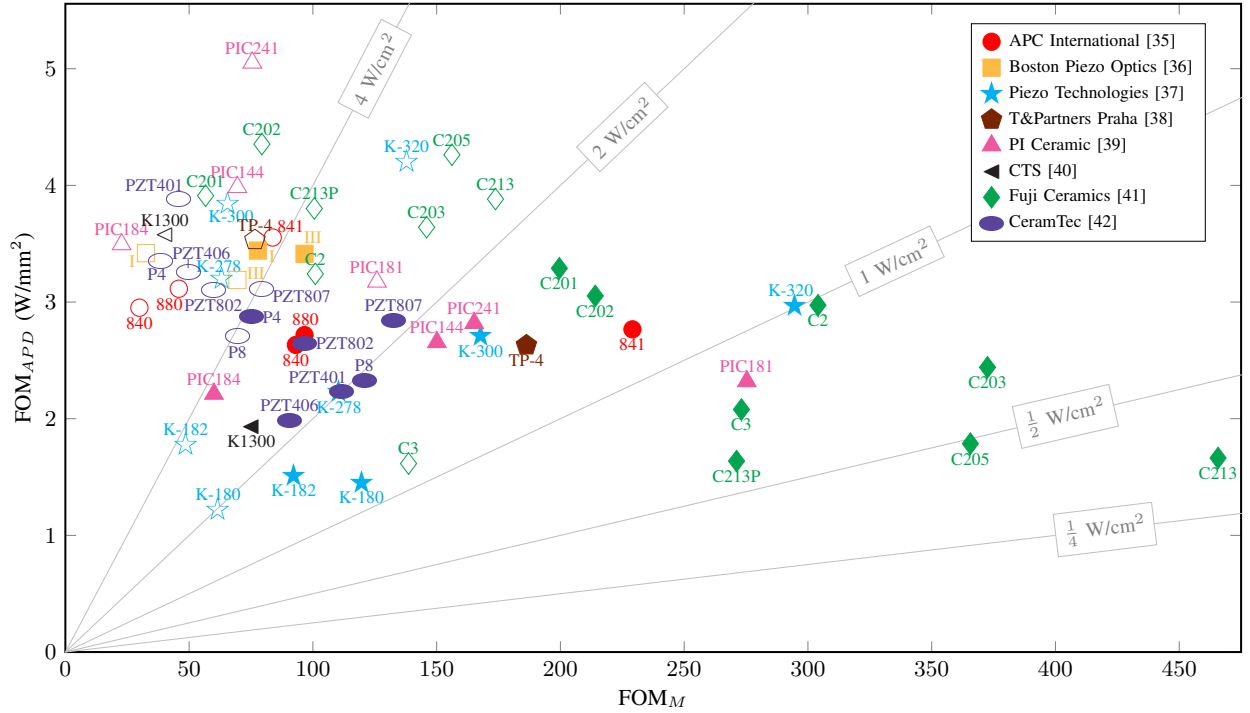
Fig. 8. Comparison of hard PZT materials for power conversion based on FOM_M and FOM_{APD}, overlaid with areal-loss-density contour lines. Filled and unfilled markers indicate the thickness shear (side electrodes) and thickness extensional vibration modes, respectively.

demonstrates higher power density capability given the same E_{max}, and thickness shear mode (denoted by filled markers) shows higher efficiency capability given the same Q_m.

Figure 8 is further overlaid with areal-loss-density contour lines to help identify thermal management limits, which vary based on design and application constraints. For a given areal loss density limit, all points above the corresponding contour line can be projected downward (in the -y direction, keeping constant FOM_M) onto the allowable heat transfer line itself; this new point conveys their maximum power densities given the assumed limit. It can be inferred that many materials would in fact never reach the assumed E_{max} limit without aggressive thermal management; for a given thermal capability, higher power density is instead enabled by a higher FOM_M. In the context of this study, this implies that the thickness shear mode enables higher power densities than the thickness extensional mode for practical areal loss density constraints (≤ 1 W/cm^2).

B. Comparing Vibration Modes

We now compare the seven vibration modes analyzed herein for hard PZT and lithium niobate using material properties from [43] and [44], respectively (we assume these properties as provided, though different crystal cuts can be similarly compared). We calculate FOM_M, FOM_{VED}, and FOM_{APD} for each vibration mode and display them in Table VII. The same Q_m and E_{max} are assumed for all modes of each material; Q_m is assumed to be 2200 for PIC181 and 10000 for LiNbO$_3$ (as reported in the datasheets), and E_{max} is assumed to be 633 V/mm for PIC181 and 7000 V/mm for LiNbO$_3$ (1/3 the coercive field of each material). An areal loss density limit of 1 W/cm^2 is also assumed, so the displayed FOMs are

based on the lower of these two limits as described in Section III(c). FOMs that have been scaled by $\frac{\widehat{G}}{4}$ or $\frac{\widehat{G}}{\pi}$ are marked with asterisks in Table VII; these FOMs assume V_{in}=100V and P_{out}=10W. For this operating point, we also display $\widehat{G}$ and a corresponding theoretical design for both maximum efficiency and maximum power density (based on $\widehat{G}$ and $\widehat{l}$) for each mode; modes for which this theoretical design violates the relative dimension assumptions in Fig. 1 are marked with "N/A".

Table VII shows the modes of each material to have significantly varying capabilities with respect to mechanical efficiency, volumetric energy handling density, and areal power density. Higher FOM_M is associated with higher k^2 (since the same Q_m is assumed for all modes of the same material), and particularly high FOM_Ms are shown for LiNbO$_3$ shear modes. Most vibration modes have loss-limited power densities as indicated by FOM_{APD} tracking FOM_M given the assumed areal loss density limit. Perpendicular vibration modes tend to have higher FOM_{VED} compared to parallel modes, which implies that perpendicular modes are capable of higher volumetric power densities for a given frequency. Also worth noting is that some modes would have to operate at more than an order of magnitude higher frequency than others to achieve the same volumetric power density.

Differences in geometry requirements are further highlighted by $\widehat{G}$ and the displayed theoretical designs. LiNbO$_3$ generally requires an order of magnitude higher $\widehat{G}$ than PZT, resulting in more planar-shaped geometries that often require more footprint area and/or higher operating frequencies for similar density. Perpendicular modes likewise require more extreme planar shapes for the same $\widehat{G}$ compared to par-

Mode	Hard PZT (PIC181)					Lithium Niobate				
	FOM_M	FOM_{VED} (J/m^3)	FOM_{APD} (W/cm^2)	$\widehat{G}^*$	Theoretical Design*	FOM_M	FOM_{VED} (J/m^3)	FOM_{APD} (W/cm^2)	$\widehat{G}^*$	Theoretical Design*
Length Ext. (s)	63.4	377	63.4	264	l=240μm, b=16mm	1.26	4.14	1.26	5190	l=390μm, b=510mm
Length Ext. (e)	345	1930	345	395	N/A	74.0	224	74.0	4910	N/A
Thickness Shear (side)	303	2740	302	553	l=77μm, $\sqrt{\frac{A}{4}}$=910μm	1810	7360	1810	4160	l=12μm, $\sqrt{\frac{A}{4}}$=370μm
Thickness Shear (end)	338	3210	337	581	l=71μm, b=10mm	2090	9110	2090	4440	l=10μm, b=12mm
Thickness Extensional	138	631	138	330	l=150μm, $\sqrt{\frac{A}{4}}$=1.3mm	72.0	198	72.0	4450	l=56μm, $\sqrt{\frac{A}{4}}$=1.9mm
Contour Extensional	229	13200	33.0*	302	l=36μm, a=2.8mm	3.14	12900*	3.14	5090	l=7μm, a=8.9mm
Radial	223	15600	52.8*	230	l=34μm, a=2.5mm	3.12	10200*	3.12	4030	l=8μm, a=10mm

*Assuming an example operating point of V_{in}=100V and P_{out}=10W. At this operating point, power density is E-field-limited only for PZT contour ext. and radial modes.

allel modes (as described in Section IV(b), parallel modes have the advantage that the length dimensions comprising $\widehat{G}$ are squared). This is less pronounced at lower $\widehat{G}$ values but more exaggerated for higher $\widehat{G}$, making parallel modes more footprint-effective for high power applications. As $\widehat{G}$ approaches infinity, all modes besides length extensional (end electrodes) are capable of designs that meet the relative dimension assumptions in Fig. 1. As $\widehat{G}$ approaches zero, the set of compatible modes reduces to just the two length extensional modes and thickness shear (end electrodes) mode.

Thus, the most appropriate piezoelectric materials and vibration modes depend heavily on the target application space. In addition to PZT and LiNbO$_3$, there are numerous other piezoelectric materials that may be similarly evaluated for power conversion using these FOMs.

VII. FIGURE OF MERIT VALIDATION

To evaluate their utility, we now validate the FOMs derived herein with numerically-obtained periodic steady state solutions (PSSS) of converter behavior and experimental results.

A. Periodic Steady State Solution

The switching sequence described in Section III(a) is assumed to operate in periodic steady state, which implies that the PR's states cycle through the same trajectories every switching cycle. As described in [5], we can quantify these trajectories in a PSSS, which varies based on circuit model parameters and operating point (V_{in}, V_{out}, and P_{out}). An "exact" PSSS (i.e., considering R in Fig. 3) can obtained by numerically solving the set of differential equations that govern the PR's states during each stage of a switching sequence. A PSSS has no dependence on the amplitude of resonance model or other derivations herein.

With an exact PSSS, we can extract useful information from the PR's state trajectories like loss and output power for validating the derived FOMs. As such, we first validate the minimum loss ratio and maximum power densities with

PSSS data based on geometry and material data for 572 APC International discrete PR parts listed on [45]; these parts consist of round and rectangular PRs of varying dimensions, spanning nine total materials. For each part, we:

1) Calculate its circuit model parameters (as shown in Table III) for a given vibration mode.
2) Based on its dimensions, determine V_{in} and P_{out} corresponding to its minimum loss ratio and maximum energy handling density using (17) and (25), assuming I_{Lmax} to be limited by an areal loss density of 1 W/cm^2.
3) For this operating point, solve for the exact PSSS of the PR's states as detailed in [5], constraining the converter switching sequence for the high-efficiency behaviors corresponding to (6) and $V_{out} = 0.55V_{in}$ (I_L is predicted to be independent of V_{out} for $V_{in} > V_{out} > \frac{1}{2}V_{in}$).
4) Extract P_{out} from the PSSS by integrating the PR's i_L trajectory during load-connected stages and then multiplying by $V_{out} \cdot f$. Extract P_{loss} from the PSSS by integrating the square of the PR's i_L trajectory during all stages and then multiplying by $R \cdot f$.

Ultimately, *all discrete parts of the same material yield the same minimum loss ratio, maximum energy handling density, and maximum areal power density for a given vibration mode*; these quantities translate directly to FOM_M, FOM_{VED}, and FOM_{APD}, respectively. In Table VIII, PSSS-calculated results for the length extensional mode (end electrodes) are compared with their derived estimates and demonstrate very small error for all low-loss-ratio materials. Accordingly, the PSSS validates the following:

- FOM_M, $\left(\frac{P_{loss}}{P_{out}}\right)_{min}$, $\widehat{G}$, and $\bar{\kappa}_o$.
- FOM_{VED}, FOM_{APD}, and $\widehat{l}$.
- The independence of $\bar{\kappa}_o$, $\left(\frac{P_{loss}}{P_{out}}\right)_{min}$, $\left(\frac{E_{out}}{\text{vol}}\right)_{max}$, $\left(\frac{P_{out}}{A_s}\right)_{max}$, and $\frac{P_{loss}}{A_s}$ from PR geometry and operating point information.
- The dependence of $\frac{E_{out}}{\text{vol}}$, $\frac{P_{out}}{A_s}$, and $\frac{P_{loss}}{A_s}$ on normalized amplitude of resonance I_{Lo}.

TABLE VIII
PSSS FIGURE OF MERIT VALIDATION

Material	Q_m	k_{33}	κ_o vs. (21) (radians)	$\frac{P_{loss}}{P_{out}}$ vs. $\frac{1}{\text{FOM}_M}$	$\frac{E_{out}}{vol}$ vs. FOM_{VED} (J/m^3)	$\frac{P_{out}}{A_s}$ vs. FOM_{APD} (W/cm^2)	$\frac{P_{loss}}{A_s}$ vs. 1.00 (W/cm^2)
840	500	0.72	1.371 | 1.364	.0102 | .0102	429.6 | 432.3	97.97 | 98.07	1.002
841	1400	0.68	1.389 | 1.385	.0041 | .0041	1073 | 1079	241.0 | 241.9	0.9912
842	600	0.71*	1.373 | 1.366	.0086 | .0086	499.3 | 502.0	116.3 | 116.3	1.001
844	1500	0.65*	1.404 | 1.405	.0043 | .0044	1009 | 1009	228.6 | 228.6	.9940
840-844 Average Error:			0.31 %	0.37%	0.45 %	0.13 %	0.43 %
880	1000	0.62	1.433 | 1.436	.0083 | .0083	523.2 | 523.7	119.5 | 120.0	.9939
881	1000	0.73*	1.360 | 1.350	.0047 | .0047	906.4 | 910.4	213.6 | 212.9	1.002
880-881 Average Error:			0.50 %	0.20%	0.26 %	0.33 %	0.39 %

Not shown: Soft PZT materials 850, 851, and 855 have loss ratios up to 0.069, with an average error (compared to (18)) of up to 6%. These materials have significantly more loss than hard PZT and are therefore less conducive to power conversion. (*) Calculated using $k_{33}^2 = Y_{33}^E d_{33}^2 / \varepsilon_{33}^T$.
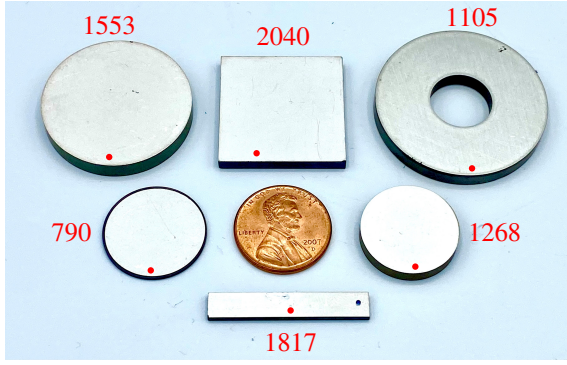

Fig. 9. PRs tested for experimental FOM validation. The wire attachment location is marked with a red dot for each PR. Parts 790 and 1817 are mounted in an upright position on the board of Fig. 10 with two wires mechanically supporting the PR as in [5]. All other PRs are positioned horizontally with the bottom electrode making contact with the copper ribbon and the other attached with a non-rigid wire.

PSSS results for all other vibration modes demonstrate similar alignment as shown in Appendix C. Thus, FOM$_M$, FOM$_{VED}$, and FOM$_{APD}$ serve as representative metrics for comparing the capabilities of low-loss piezoelectric materials.

B. Experimental Results

We further validate the mechanical efficiency FOM experimentally using six of the PR parts considered in Section VII. These PRs consist of APC International's highest-FOM$_M$ materials (841, 844, 880, and 881) in different shapes and sizes as pictured in Fig. 9. These parts are selected to be low in frequency (< 600 kHz) to minimize frequency-dependent loss and potential damping effects due to mounting during validation. With each PR, we perform the following:

1) Plot the PR's impedance characteristic (i.e., Fig. 2) for a given vibration mode using an impedance analyzer.
2) Estimate Q_m, k, and C_p based on the impedance characteristic, as detailed in Appendix D.
3) Calculate the minimum loss ratio for the estimated Q_m and k using (18). Calculate the minimum-loss-ratio P_{out} using (17), assuming $V_{in} = 100$ V and charge-equivalent switch capacitances of 250 pF (requiring 500 pF total to be added to C_p) [46].
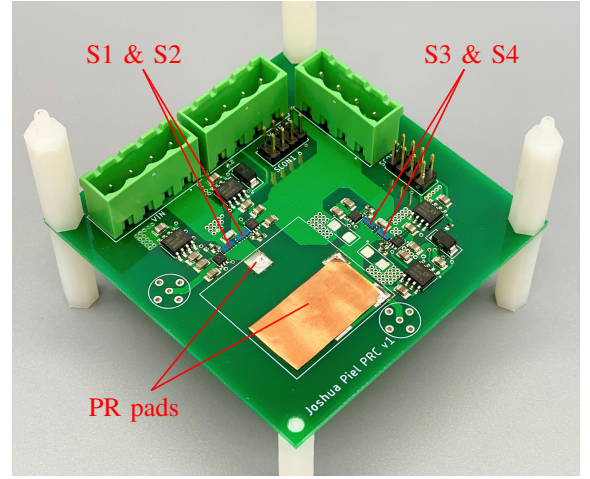

Fig. 10. Experimental prototype board, re-purposed from [5]. All switches are EPC 2019 GaN FETs, driven with Texas Instruments UCC27611 gate drivers. An isolated supply powers the gate circuitry for S1 and S2.

4) Run the PR in the prototype converter shown in Fig. 10 with the V_{in}-V_{out}, *Zero*, V_{out} switching sequence, constrained for the high-efficiency behaviors assumed in Section III(a). This prototype and switching sequence have the topology and waveforms of Fig. 4 and 5, respectively. $V_{in} = 100$ V and $V_{out} = 60$ V, implemented with a constant-voltage load. All switching times are feed-forward and manually tuned; for a given V_{in}, V_{in}, and P_{out}, there is a unique tuning point that satisfies the assumptions of Section III.
5) Sweep through multiple power levels surrounding the calculated P_{out} to identify the minimum loss ratio and corresponding P_{in}, P_{out}, and f, maintaining the same V_{in} and V_{out} and re-tuning switching times as needed for the high-efficiency behaviors assumed in Section III.

The results of these experiments, along with material, vibration mode, and frequency information for each PR, are displayed in Table IX. The estimated PR loss ratio (or $\frac{1}{\text{FOM}_M}$) tracks the trend of the experimental whole-converter loss ratio as visualized in Fig. 11, albeit a slight underestimation. Sources for the observed discrepancies include other circuit

TABLE IX
EXPERIMENTAL FIGURE OF MERIT VALIDATION

Part No.	Material	Vibration Mode	Q_m	k	C_p (nF)	f vs. (20) (kHz)	P_{out} vs. (17) (W)	$\frac{P_{loss}}{P_{out}}$ vs. $\frac{1}{\text{FOM}_M}$ (PR only)	Efficiency
1817	841	Length Ext. (s)	700	.32	.993	56.8 | 56.7	0.59 | 0.85	.0559 | .0503	94.7 %
1105	841	Thickness Ext.	2500	.31	.602	605 | 596	4.0 | 6.6	.0221 | .0156	97.8 %
2040	880	Contour Ext.	1600	.52	1.64	81.1 | 80.9	1.6 | 1.7	.0101 | .0069	99.0 %
1553	841	Radial	1700	.58	1.50	80.9 | 80.9	1.6 | 1.6	.0080 | .0049	99.2 %
790	844	Radial	1400	.55	3.53	124 | 122	4.1 | 4.9	.0090 | .0069	99.1 %
1268	881	Radial	1600	.52	.643	129 | 129	1.3 | 1.5	.0088 | .0072	99.1 %

In this table, Q_m, k, and C_p are obtained by PR characterization. (20), (17), and $\frac{1}{\text{FOM}_M}$ are calculated using these characterized quantities along with characterized f_r and f_{ar} and other manufacturer-provided material properties. f, P_{out}, $\frac{P_{loss}}{P_{out}}$, and efficiency are measured during operation of the converter prototype at its minimum loss ratio.
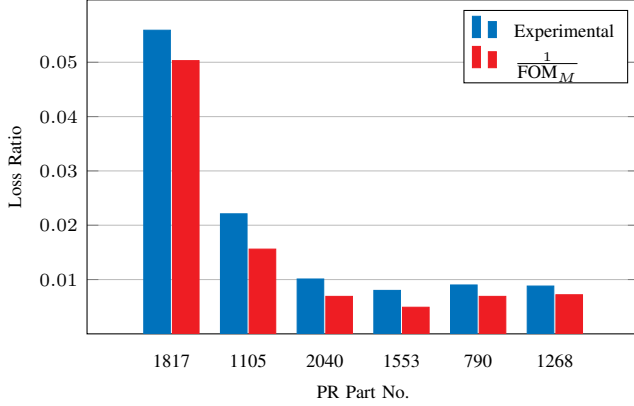

Fig. 11. Experimental (whole-converter) minimum loss ratio compared to $\frac{1}{\text{FOM}_M}$ for the PRs of Fig. 9, operated in the converter prototype of Fig. 10.

TABLE X
PIEZOELECTRIC RESONATOR SCALING PROPERTIES

Property	Geometry Dependence	Scaling (fixed I_{Lo})
$\left(\frac{P_{out}}{vol}\right)$ (23)	G_f	α^{-1}
$\left(\frac{E_{out}}{vol}\right)_{max}$ (26)	none	constant
$\left(\frac{P_{out}}{A_s}\right)_{max}$ (30)	none	constant
$\left(\frac{P_{loss}}{P_{out}}\right)_{min}$ (18)	none	constant
$\frac{P_{loss}}{A_s}$ (10)	none	constant
f (3)	G_f	α^{-1}

losses (e.g., switch loss), as well as differences between the PR's small-signal (as characterized) and large-signal (as tested) characteristics. Thus, (18) provides a close approximation of the loss ratio to be expected by a given material and vibration mode, validating the utility of FOM_M.

VIII. FUNDAMENTAL SCALING PROPERTIES

PRs have been previously suggested to have advantageous power density and efficiency scaling properties compared to magnetics [4]. Equipped with our FOM derivations, we explore how PR capabilities scale with size for the realistic converter operation assumed for this work.

If a PR is scaled in all three dimensions by linear scaling factor α as postulated for magnetics in [2], its volume scales by α^3. In the case of a PR with fixed I_{Lo}, maximum volumetric power density scales inversely with α as does operating frequency, both due to G_f. However, the minimum loss ratio, the maximum volumetric energy handling density, the maximum areal power density, and the areal loss density have *no geometry dependence* and therefore remain fixed regardless of α. Table X summarizes these characteristics.

Thus, as volume is scaled downward ($\alpha < 1$), maximum volumetric power density increases while minimum loss ratio (and therefore maximum efficiency) stays constant. These are favorable scaling properties for converter miniaturization.

IX. CONCLUSIONS

To evaluate piezoelectric materials and vibration modes for power conversion, we have established FOMs for achievable efficiency (FOM_M), volumetric energy handling density (FOM_{VED}), and areal power density (FOM_{APD}) based on realistic PR utilization in a converter. These FOMs depend on only material properties and areal loss density limits (if considered), and they correspond to PR geometry conditions $\widehat{G}$ and $\widehat{l}$ for realizing both maximum efficiency and maximum power density in a PR design.

The derived FOM_M depends on only k^2 and Q_m, and its corresponding geometry condition $\widehat{G}$ dictates the relative PR dimensions corresponding to maximum efficiency for a given operating point. Parallel modes are particularly advantageous for satisfying $\widehat{G}$ with less-extreme planar shapes. Which vibration modes are compatible with a given operating space is likewise dictated by $\widehat{G}$, favoring vibration modes with l as their smallest dimensions for most realistic converter applications. Further, the operating frequency at which maximum efficiency occurs is found to be the geometric mean of the PR's resonant and anti-resonant frequencies for the assumed operation.

The derived FOM_{VED} and FOM_{APD} are constrained by the PR's geometry-normalized amplitude of resonance I_{Lmaxo}, which can be calculated based on material limits or an acceptable areal loss density. FOM_{VED} is normalized to frequency, which permits direct comparison between vibration modes for a given converter switching and control requirement. FOM_{APD} provides insight into footprint requirements for planar-shaped PRs, though the utility of this FOM depends on whether its assumed area corresponds to the footprint area of a given PR configuration; some modes require scaling by

a multiple of $\frac{1}{\widehat{G}}$ for a representative footprint density. Both of these FOMs have the same geometry condition $\widehat{l}$ for maximum power density at a given operating point.

We illustrate the utility of the proposed FOMs to compare the capabilities of 30 PZT-based materials and seven PR vibration modes for PZT and lithium niobate. These materials and vibration modes vary immensely with respect to the FOMs, though higher FOM_M often enables higher power densities for realistic areal loss density limits. With the same Q_m assumed for each mode, the shear modes demonstrate the highest FOM_M, particularly for lithium niobate. Perpendicular modes are generally capable of higher FOM_{VED} but tend to be more planar, requiring more footprint area than parallel modes to satisfy $\widehat{G}$. Lithium niobate also necessitates more extreme planar dimensions than PZT to meet $\widehat{G}$, requiring more footprint area and/or higher frequency for the same volumetric power density.

We validate these FOMs and their geometry conditions using a periodic steady state numerical solver and experimental results with commercially-available PTs. All PRs of the same material and vibration mode yield the same minimum loss ratio, maximum energy handling density, and maximum areal power density for a given areal loss density, validating the independence of these quantities from PR geometry and operating point information. The proposed FOMs are demonstrated to be highly representative metrics for the achievable efficiencies and power densities of piezoelectric materials and vibration modes, and their corresponding geometry conditions are verified to facilitate both maximum efficiency and maximum power density in a PR design. Further, the displayed FOM values throughout this work attest to the aptitude of piezoelectrics for power conversion in terms of efficiency and power density capabilities, which are shown to scale favorably for converter miniaturization.

ACKNOWLEDGMENT

APPENDIX A
PIEZOELECTRIC RESONATOR WAVE SOLUTION

In this Appendix, we derive the PR's acoustic wave solution for each vibration mode. Piezoelectric materials are governed by the constitutive relations in (1)-(2) and equation of motion

$$\nabla \cdot \mathbf{T} = \rho \ddot{\mathbf{u}}, \tag{32}$$

along with strain-displacement definition $\mathbf{S} = \frac{1}{2}(\nabla \mathbf{u} + \mathbf{u}\nabla)$ and Gauss's Law $\nabla \cdot \mathbf{D} = 0$. Together, these equations determine the behavior of the PR states, which varies by vibration mode.
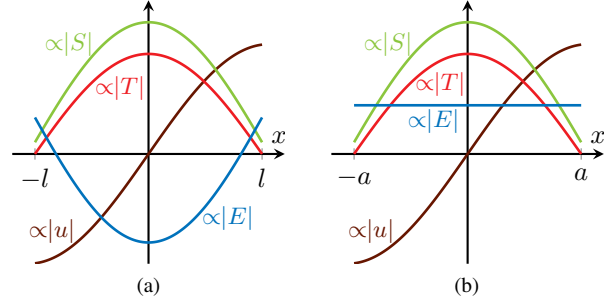

Fig. 12. Relative amplitudes of u, S, T, and E along the axis of G_f in a PR for (a) vibration modes in which the applied and induced E fields are parallel ($\parallel$) and (b) vibration modes in which the applied and induced E fields are perpendicular ($\perp$).

TABLE XI
PARAMETERS FOR EACH VIBRATION MODE [29]

Mode	v_a	d	s^E	ε^T	k
Length Ext. (s)	$\sqrt{\dfrac{1}{\rho s_{11}^E}}$	d_{31}	s_{11}^E	ε_{33}^T	$k_{31}=\dfrac{d_{31}}{\sqrt{s_{11}^E \varepsilon_{33}^T}}$
Length Ext. (e)	$\sqrt{\dfrac{1}{\rho s_{33}^D}}$	d_{33}	s_{33}^E	ε_{33}^T	$k_{33}=\dfrac{d_{33}}{\sqrt{s_{33}^E \varepsilon_{33}^T}}$
Thickness shear (side)	$\sqrt{\dfrac{1}{\rho s_{55}^D}}$	d_{15}	s_{55}^E	ε_{11}^T	$k_{15}=\dfrac{d_{15}}{\sqrt{s_{55}^E \varepsilon_{11}^T}}$
Thickness shear (end)	$\sqrt{\dfrac{1}{\rho s_{55}^E}}$	d_{15}	s_{55}^E	ε_{11}^T	$k_{15}=\dfrac{d_{15}}{\sqrt{s_{55}^E \varepsilon_{11}^T}}$
Thickness Extensional	$\sqrt{\dfrac{c_{33}^D}{\rho}}$	**	**	**	$k_t=\dfrac{e_{33}}{\sqrt{c_{33}^D \varepsilon_{33}^S}}$
Contour Extensional	$\sqrt{\dfrac{1}{\rho s_{11}^E(1-\sigma^2)}}$	d_{31}	s_{11}^E	ε_{33}^T	$k_p=\sqrt{\dfrac{2k_{31}^2}{1-\sigma}}$
Radial	$\sqrt{\dfrac{1}{\rho s_{11}^E(1-\sigma^2)}}$	d_{31}	s_{11}^E	ε_{33}^T	$k_p=\sqrt{\dfrac{2k_{31}^2}{1-\sigma}}$

Measurement condition conversions [29]:

$\varepsilon_{11}^S = (1 - k_{15}^2)\varepsilon_{11}^T \quad \varepsilon_{33}^S = (1 - k_{33}^2)\varepsilon_{33}^T \quad s_{11}^D = (1 - k_{31}^2)s_{11}^E$

$s_{33}^D = (1 - k_{33}^2)s_{33}^E \quad s_{55}^D = (1 - k_{15}^2)s_{55}^E \quad c_{33}^E = (1 - k_t^2)c_{33}^D$

**Thickness extensional mode is commonly represented by e_{33}, c_{33}^E, and ε_{33}^S.

A. One-Dimensional Stress/Strain Modes

Most vibration modes considered (length extensional, thickness shear, and thickness extensional) can be modeled by one-dimensional stress/strain (i.e., we consider only one tensor component for each PR state in (1)-(2), (32)). For this case, the coupled constitutive relations take the reduced form:

$$S = s^E T + dE \tag{33}$$

$$D = dT + \varepsilon^T E \tag{34}$$

To illustrate the PR behaviors for each vibration mode, we adopt a generalized notation for all parameters without indices; the tensor components pertinent to each vibration mode (using Voigt notation) are displayed in Table XI. We likewise refer to a location along the l-dimension axis for parallel modes and a-dimension axis for perpendicular modes as generally "x".

With the equation of motion (32), (33)-(34) create an acoustic wave equation for mechanical displacement u:

$$\frac{\partial^2 u}{\partial t^2} = v_a^2 \frac{\partial^2 u}{\partial x^2} \tag{35}$$

TABLE XII
ONE-DIMENSIONAL VIBRATION MODE DERIVATIONS

	Length Ext. (s) and Thickness Shear (e)	Length Ext. (e) and Thickness Shear (s)	Thickness Extensional
S	$\kappa\Delta\cos(\kappa x)e^{j\omega t}$	$\kappa\Delta\cos(\kappa x)e^{j\omega t}$	$\kappa\Delta\cos(\kappa x)e^{j\omega t}$
T	$\frac{1}{s^E}\kappa\Delta\left(\cos(\kappa x)-\cos(\kappa_o)\right)e^{j\omega t}$	$\frac{1}{s^D}\kappa\Delta\left(\cos(\kappa x)-\cos(\kappa_o)\right)e^{j\omega t}$	$c^D\kappa\Delta\left(\cos(\kappa x)-\cos(\kappa_o)\right)e^{j\omega t}$
E	$\frac{\kappa\Delta}{d}\left(\cos(\kappa_o)\right)e^{j\omega t}$	$\frac{\kappa\Delta}{d(1-k^2)}\left(-k^2\cos(\kappa x)+\cos(\kappa_o)\right)e^{j\omega t}$	$\frac{c^D\kappa\Delta}{e(1-k^2)}\left(-k^2\cos(\kappa x)+\cos(\kappa_o)\right)e^{j\omega t}$
I_L	$\kappa AG_f\frac{v_a d}{s^E}\Delta\sin(\kappa_o)$	$\kappa AG_f\frac{v_a d}{s^E}\Delta\sin(\kappa_o)$	$\kappa AG_f v_a e\Delta\sin(\kappa_o)$
Δ_S	$\frac{1}{\kappa}S_{max}$	$\frac{1}{\kappa}S_{max}$	$\frac{1}{\kappa}S_{max}$
Δ_T	$\frac{s^E}{\kappa}\frac{1}{1-\cos(\kappa_o)}T_{max}$	$\frac{s^D}{\kappa}\frac{1}{1-\cos(\kappa_o)}T_{max}$	$\frac{1}{c^D\kappa}\frac{1}{1-\cos(\kappa_o)}T_{max}$
Δ_E	$\frac{d}{\kappa}\frac{1}{\cos(\kappa_o)}E_{max}$	$\frac{d}{\kappa}\frac{(1-k^2)}{(\cos(\kappa_o)-k^2)}E_{max}$	$\frac{e}{c^D\kappa}\frac{1}{(\cos(\kappa_o)-k^2)}E_{max}$
I_{LmaxS}	$AG_f\frac{v_a d}{s^E}S_{max}\sin(\kappa_o)$	$AG_f e v_a S_{max}\sin(\kappa_o)$	$AG_f\frac{v_a d}{s^E}S_{max}\sin(\kappa_o)$
I_{LmaxT}	$AG_f v_a d T_{max}\cot(\frac{\kappa_o}{2})$	$AG_f v_a d(1-k^2)T_{max}\cot(\frac{\kappa_o}{2})$	$AG_f v_a\frac{e}{c^D}T_{max}\cot(\frac{\kappa_o}{2})$
I_{LmaxE}	$AG_f k^2\varepsilon^T v_a E_{max}\tan(\kappa_o)$	$AG_f k^2\varepsilon^S v_a E_{max}\frac{\sin(\kappa_o)}{\cos(\kappa_o)-k^2}$	$AG_f k^2\varepsilon^S v_a E_{max}\frac{\sin(\kappa_o)}{\cos(\kappa_o)-k^2}$

TABLE XIII
PLANAR VIBRATION MODE DERIVATIONS

	Contour Extensional	Radial
S	$S_1=\kappa\Delta\cos(\kappa x_1)e^{j\omega t}$ $S_2=\kappa\Delta\cos(\kappa x_2)e^{j\omega t}$	$S_{rr}=\frac{\kappa}{2}\Delta(J_0(\kappa r)-J_2(\kappa r))e^{j\omega t}$ $S_{\theta\theta}=\frac{1}{r}\Delta J_1(\kappa r)e^{j\omega t}$
T	$T_1=\frac{\kappa\Delta e^{j\omega t}}{s_{11}^E(1-\sigma^2)}\left(\cos(\kappa x_1)+\sigma\cos(\kappa x_2)-(1+\sigma)\cos(\kappa_o)\right)$ $T_2=\frac{\kappa\Delta e^{j\omega t}}{s_{11}^E(1-\sigma^2)}\left(\sigma\cos(\kappa x_1)+\cos(\kappa x_2)-(1+\sigma)\cos(\kappa_o)\right)$	$T_{rr}=\frac{\Delta e^{j\omega t}}{s_{11}^E(1-\sigma^2)}\left(\frac{\kappa}{2}\left(J_0(\kappa r)-J_2(\kappa r)\right)+\frac{\sigma}{r}J_1(\kappa r)-\kappa\Psi\right)$ $T_{\theta\theta}=\frac{\Delta e^{j\omega t}}{s_{11}^E(1-\sigma^2)}\left(\frac{\kappa\sigma}{2}\left(J_0(\kappa r)-J_2(\kappa r)\right)+\frac{1}{r}J_1(\kappa r)-\kappa\Psi\right)$
E	$\frac{\kappa\Delta}{d_{31}}\left(\cos(\kappa_o)\right)e^{j\omega t}$	$\frac{\kappa\Delta}{d_{31}(1+\sigma)}\Psi e^{j\omega t}$
I_L	$2\kappa AG_f\frac{v_a d_{31}}{s_{11}^E(1-\sigma)}\Delta\sin(\kappa_o)$	$\kappa_o v_a\frac{2\pi d_{31}}{s_{11}^E(1-\sigma)}\Delta J_1(\kappa_o)$
Δ_S	$\frac{1}{\kappa}S_{max}$	$\frac{2}{\kappa}S_{max}$
Δ_T	$\frac{s_{11}^E(1-\sigma)}{\kappa(1-\cos(\kappa_o))}T_{max}$	$\frac{s_{11}^E(1-\sigma^2)}{\kappa(\frac{1}{2}(1+\sigma)-\Psi)}T_{max}$
Δ_E	$\frac{d_{31}}{\kappa}\frac{1}{\cos(\kappa_o)}E_{max}$	$\frac{d_{31}(1+\sigma)}{\kappa\Psi}E_{max}$
I_{LmaxS}	$2AG_f v_a\frac{d_{31}}{s_{11}^E(1-\sigma)}S_{max}\sin(\kappa_o)$	$AG_f\frac{4d_{31}v_a}{s_{11}^E(1-\sigma)}S_{max}J_1(\kappa_o)$
I_{LmaxT}	$2AG_f v_a d_{31}T_{max}\cot(\frac{\kappa_o}{2})$	$AG_f\frac{2v_a d_{31}(1+\sigma)}{\frac{1}{2}(1+\sigma)-\Psi}T_{max}J_1(\kappa_o)$
I_{LmaxE}	$AG_f v_a k_p^2\varepsilon_{33}^T E_{max}\tan(\kappa_o)$	$AG_f v_a k_p^2\varepsilon_{33}^T(1+\sigma)E_{max}\frac{J_1(\kappa_o)}{\Psi}$

The PR is assumed to resonate in the proximity of its lowest-frequency vibration mode for traction-free boundaries in Fig. 1. Thus, the acoustic wave solution is sinusoidal in form:

$$u = \Delta\sin(\kappa x)e^{j\omega t} \tag{36}$$

Inserting (36) into the constitutive relations and enforcing traction-free boundaries yields the solutions for S, T, and E; these solutions are displayed for each mode in Table XII. Fig. 12 illustrates the relative amplitudes of u, S, T, and E. These states retain similar spacial dependencies across x for each vibration mode, though their specific directions may be different. Moreover, the maximum amplitudes for S, T, and E each occur at the center of the PR (at $x=0$).

This wave solution provides means to analyze the PR's mechanical and electrical limits, which we utilize in Section V and Appendix B. Also, the Butterworth-Van Dyke circuit model (Fig. 3) can be derived from E as detailed in [29].

B. Contour Extensional Mode

For contour extensional mode, we assume the PR to be under plane stress (i.e., we consider only the normal stress components along the two axes perpendicular to the applied E field). We denote these normal stresses with T_1 and T_2, and their coordinate plane is defined by the red displacement lines in Fig. 1(f) with the origin at the center of the PR. The constitutive relations then have the form [29]:

$$T_1 = \frac{1}{s_{11}^E(1-\sigma^2)}\left(\frac{\partial u_1}{\partial x_1}+\sigma\frac{\partial u_2}{\partial x_2}\right) - \frac{d_{31}}{s_{11}^E(1-\sigma)}E \tag{37}$$

$$T_2 = \frac{1}{s_{11}^E(1-\sigma^2)}\left(\sigma\frac{\partial u_1}{\partial x_1}+\frac{\partial u_2}{\partial x_2}\right) - \frac{d_{31}}{s_{11}^E(1-\sigma)}E \tag{38}$$

$$D = \frac{d_{31}}{s_{11}^E(1-\sigma)}\left(\frac{\partial u_1}{\partial x_1}+\frac{\partial u_2}{\partial x_2}\right) + \varepsilon_{33}^T(1-k_p^2)E \tag{39}$$

With (32), these equations constitute an acoustic wave equation for mechanical displacement u. Its solution can be approximated by two separate waves, which we assume to be identical along their respective dimensions [29]:

$$u_1 = \Delta\sin(\kappa x_1)e^{j\omega t} \tag{40}$$

$$u_2 = \Delta\sin(\kappa x_2)e^{j\omega t} \tag{41}$$

TABLE XIV
BESSEL FUNCTION EXPANSIONS

Function	Expansion Around $\kappa_o = 2$
$\kappa_o \frac{J_0(\kappa_o)}{J_1(\kappa_o)}$	$0.776 - 1.525(\kappa_o - 2) - 0.789(\kappa_o - 2)^2$
$J_0(\kappa_o)$	$0.224 - 0.577(\kappa_o - 2) - 0.0322(\kappa_o - 2)^2$
$J_1(\kappa_o)$	$0.577 - 0.645(\kappa_o - 2) - 0.2(\kappa_o - 2)^2$
$J_2(\kappa_o)$	$0.353 - 0.224(\kappa_o - 2) - 0.0560(\kappa_o - 2)^2$

TABLE XV
CIRCUIT MODEL PARAMETERS FOR RADIAL VIBRATION MODE [29]

Parameter	Radial Mode Expression
G_f	$\frac{1}{a}$
C_p	$\varepsilon^T (1 - k_p^2) \frac{A}{2l}$
C	$\frac{2(1+\sigma)}{\kappa_{o,r}^2 - (1-\sigma^2)} \frac{k_p^2}{1-k_p^2} C_p$
L	$\frac{1}{2G_f^2 v_a^2 C_p} \frac{1-k_p^2}{k_p^2} \frac{\kappa_{o,r}^2 - (1-\sigma^2)}{\kappa_{o,r}^2 (1+\sigma)}$
R	$\frac{1}{Q_m} \sqrt{\frac{L}{C}}$

Inserting (40) and (41) into (37) and (38) and enforcing the boundary conditions of $T_1 = 0$ at $x_1 = \pm a$ and $T_2 = 0$ at $x_2 = \pm a$ provides the analytical solution shown in Table XIII for the PR's S, T, and E states. This solution follows the relative amplitudes illustrated in Fig. 12(b).

C. Radial Mode

For the radial vibration mode, we assume only planar stress components parallel to the electrodes; E is again applied only in the polarization direction. This time, we adopt a cylindrical coordinate system in which r is the radial coordinate and θ is the hoop coordinate. Thus, the constitutive relations are [29]:

$$T_{rr} = \frac{1}{s_{11}^E(1 - \sigma^2)} \left(\frac{\partial u_r}{\partial r} + \sigma \frac{u_r}{r} \right) - \frac{d_{31}}{s_{11}^E(1 - \sigma)} E \quad (42)$$

$$T_{\theta\theta} = \frac{1}{s_{11}^E(1 - \sigma^2)} \left(\sigma \frac{\partial u_r}{\partial r} + \frac{u_r}{r} \right) - \frac{d_{31}}{s_{11}^E(1 - \sigma)} E \quad (43)$$

$$D = \frac{d_{31}}{s_{11}^E(1 - \sigma)} \left(\frac{\partial u_r}{\partial r} + \frac{u_r}{r} \right) + \varepsilon_{33}^T(1 - k_p^2) E \quad (44)$$

Together with the equation of motion (32), these constitute a wave equation for mechanical displacement u_r with solution

$$u_r = \Delta J_1(\kappa r) e^{j\omega t} \quad (45)$$

for which J_n is the Bessel function of first kind and nth order. Inserting (45) into (42) and enforcing the boundary condition $T_{rr} = 0$ at $r = a$ yields the analytical solution in Table XIII for the PR's S, T, and E states, which follows the illustration in Fig. 12(b) for $x = r$. In this solution, we have substituted

$$\Psi = \frac{1}{2} J_0(\kappa_o) - \frac{1}{2} J_2(\kappa_o) + \frac{\sigma}{\kappa_o} J_1(\kappa_o) \quad (46)$$

The geometry-normalized wave numbers corresponding to f_r and f_{ar} in radial mode are solutions to the following transcendental equations, respectively [29]:

$$\kappa_{o,r} \frac{J_0(\kappa_{o,r})}{J_1(\kappa_{o,r})} = 1 - \sigma \quad (47)$$

$$\kappa_{o,ar} \frac{J_0(\kappa_{o,ar})}{J_1(\kappa_{o,ar})} = 1 - \sigma - \frac{k_p^2}{1 - k_p^2}(1 + \sigma) \quad (48)$$

If needed, Bessel functions $J_0(\kappa_o)$, $J_1(\kappa_o)$, and $J_2(\kappa_o)$ can be approximated by series expansions around $\kappa_{o,r}$; second-order expansions around $\kappa_o = 2$ are shown in Table XIV. The geometry-normalized wave number that corresponds to the minimum-loss-ratio operating frequency is then:

$$\bar{\kappa}_o = \frac{2\kappa_{o,r}\kappa_{o,ar}}{\kappa_{o,r} + \kappa_{o,ar}} \quad (49)$$

Finally, E in Table XIII can be reduced to the circuit model of Fig. 3 with the parameters shown in Table XV.

APPENDIX B
MAXIMUM IL DERIVATION

In this Appendix, we determine the maximum permissible I_L based on limits for the PR's S, T, and E states. To begin, we derive the relationship between I_L and the PR's maximum displacement amplitude (Δ) using constitutive relations (1)-(2) and our solutions in Tables XII-XIII. For a one-dimensional vibration mode, inserting (33) into (34) yields:

$$D = \frac{d}{s^E} \frac{\partial u}{\partial x} + \varepsilon^T \left(1 - k^2 \right) E \quad (50)$$

Integrating across the volume of the PR (i.e., across electrode area A and distance $2l$) gives:

$$Q = AG_f \frac{d}{s^E} u(G_f^{-1}) + \frac{A}{2l} \varepsilon^T \left(1 - k^2 \right) v_{p,1} \quad (51)$$

for which $v_{p,1}$ is the first harmonic approximation of v_p. Finally, taking the time derivative yields:

$$i_{in} = j\omega AG_f \frac{d}{s^E} u(G_f^{-1}) + C_p \frac{dv_{p,1}}{dt} \quad (52)$$

in which i_{in} can be considered the current entering the PR through its top terminal as modeled in Fig. 3. For planar modes, this process results in a similar form as (52) for contour extensional mode and the following form for radial mode:

$$i_{in} = j\omega a \frac{2\pi d_{31}}{s_{11}^E(1 - \sigma)} \Delta J_1(\kappa_o) e^{j\omega t} + C_p \frac{dv_{p,1}}{dt} \quad (53)$$

These expressions for i_{in} correspond to Fig. 3 such that I_L equals the magnitude of the first term in (52) or (53). I_L is shown for each operating mode in Tables XII and XIII.

From here, S, T and E can each be related to I_L through Δ. As shown in Fig. 12, the maximum S, T and E each occur at $x = 0$, so we rearrange their respective equations in Tables XII-XIII and focus on $x = 0$ to reach Δ_S, Δ_T, and Δ_E as functions of S_{max}, T_{max} and E_{max}, respectively (S_{max} and T_{max} refer to the maximum principal strains and stresses for planar modes; this requires taking the limit as $r \to 0$ for radial mode). Each Δ can then be directly inserted into I_L, resulting in the strain-limited (I_{LmaxS}), stress-limited (I_{LmaxT}), and E-field-limited (I_{LmaxE}) maximum amplitudes of resonance displayed in Tables XII-XIII. I_{LmaxS}, I_{LmaxT}, and I_{LmaxE} all have the same geometry terms (AG_f), which allows direct comparison of their geometry-normalized quantities.

TABLE XVI
EXTENDED FIGURE OF MERIT VALIDATION USING APC INTERNATIONAL PZT PARTS [35]

Vibration Mode	Material	$\frac{P_{loss}}{P_{out}}$ vs. $\frac{1}{\text{FOM}_M}$	κ_o vs. (21) (radians)	$\frac{E_{out}}{\text{vol}}$ vs. FOM_{VED} (J/m³)	$\frac{P_{out}}{A_s}$ vs. FOM_{APD} (W/cm²)	$\frac{P_{loss}}{A_s}$ vs. 1.00 (W/cm²)
Length Ext. (side)	840	.0602 | .0570	1.607 | 1.613	112.3 | 112.1	17.52 | 17.54	1.054
	841	.0236 | .0232	1.603 | 1.608	248.5 | 247.8	43.12 | 43.13	1.018
	880	.0414 | .0399	1.597 | 1.601	142.0 | 142.4	24.91 | 25.04	1.032
Thickness Shear (side)	840	.0108 | .0107	1.379 | 1.373	803.2 | 809.4	92.80 | 93.14	.9992
	841	.0043 | .0044	1.395 | 1.394	1986 | 1979	230.1 | 229.1	.9984
	880	.0103 | .0103	1.455 | 1.461	840.2 | 836.3	96.68 | 96.62	1.000
Thickness Shear (end)	840	.0093 | .0092	1.810 | 1.795	1004 | 1009	108.7 | 108.4	1.006
	841	.0038 | .0038	1.776 | 1.769	2377 | 2396	260.2 | 261.3	.9918
	880	.0096 | .0096	1.683 | 1.689	938.2 | 932.8	104.3 | 104.1	1.001
Thickness Extensional	842	.0243 | .0240	1.483 | 1.490	195.1 | 193.5	41.88 | 41.70	1.019
	844	.0096 | .0096	1.483 | 1.490	485.5 | 483.6	104.2 | 104.3	.9999
	881	.0160 | .0159	1.491 | 1.497	293.8 | 293.2	62.79 | 62.94	1.005
Contour Extensional	840	.0159 | .0158	1.708 | 1.712	271.8 | 272.4	62.96 | 63.22	1.001
	841	.0054 | .0054	1.715 | 1.718	826.1 | 826.7	185.3 | 185.8	.9921
	880	.0124 | .0123	1.658 | 1.665	362.1 | 361.2	80.99 | 81.16	1.000
Radial	840	.0163 | .0161	2.221 | 2.092	269.5 | 271.0	62.3 | 62.30	1.014
	841	.0056 | .0056	2.292 | 2.276	809.5 | 811.1	180.1 | 180.1	1.008
	880	.0126 | .0125	2.147 | 2.148	355.4 | 357.0	79.45 | 79.85	1.002

APPENDIX C
EXTENDED PSSS VALIDATION RESULTS

PSSS results validating the length extensional mode (end electrodes) FOMs are shown in Table VIII. Results for all other considered modes are displayed in Table XVI. The energy and power density quantities are validated for all materials based on areal loss density constraint (10), though the practical relevance of considered area A_s in this calculation depends on the specific vibration mode and mounting structure.

APPENDIX D
PR CHARACTERIZATION FOR EXPERIMENTAL VALIDATION

For experimental validation, we first characterize each PR in order to calculate its FOMs based on physical properties. Q_m can be calculated based on the PR's 3dB bandwidth at resonance as measured using an impedance analyzer [29]:

$$Q_m = \frac{f_r}{\text{BW}_{3dB}} \tag{54}$$

Further, the effective k can be calculated based on the observed resonant and anti-resonant frequencies:

$$k_{eff} = \sqrt{\frac{f_{ar}^2 - f_r^2}{f_{ar}^2}} \tag{55}$$

This enables the following mode-specific k calculations [29]:

$$k_{||}^2 = \frac{\pi}{2}\sqrt{1 - k_{eff}^2}\cot(\frac{\pi}{2}\sqrt{1 - k_{eff}^2}) \tag{56}$$

$$k_+^2 = \frac{1}{1 - \frac{2}{\pi}\sqrt{1 - k_{eff}^2}\tan(\frac{\pi}{2}\frac{1}{\sqrt{1 - k_{eff}^2}})} \tag{57}$$

$$k_{p(radial)}^2 = \frac{(1 - \sigma)J_1(\kappa_{ar}) - \kappa_{ar}J_0(\kappa_{ar})}{2J_1(\kappa_{ar}) - \kappa_{ar}J_0(\kappa_{ar})} \tag{58}$$

C_p and other circuit parameters can be extracted by matching Fig. 3 to the impedance characteristic.

REFERENCES

[1] J. D. Boles, P. L. Acosta, Y. K. Ramadass, J. H. Lang, and D. J. Perreault, "Evaluating piezoelectric materials for power conversion," in *Proc. IEEE Workshop on Control and Modeling for Power Electronics*, Aalborg, Denmark, Nov. 2020, pp. 1–8.

[2] C. R. Sullivan, B. A. Reese, A. L. Stein, and P. A. Kyaw, "On size and magnetics: Why small efficient power inductors are rare," in *Proc. IEEE Intl. Symposium on 3D Power Electronics Integration and Manufacturing*, Raleigh, NC, USA, Jun. 2016, pp. 1–23.

[3] D. J. Perreault, J. Hu, J. M. Rivas, Y. Han, O. Leitermann, R. C. Pilawa-Podgurski, A. Sagneri, and C. R. Sullivan, "Opportunities and challenges in very high frequency power conversion," in *Proc. IEEE Applied Power Electronics Conference and Exposition*, Washington, DC, USA, Feb. 2009, pp. 1–14.

[4] P. A. Kyaw, A. L. Stein, and C. R. Sullivan, "Fundamental examination of multiple potential passive component technologies for future power electronics," *IEEE Transactions on Power Electronics*, vol. 33, no. 12, pp. 10,708–10,722, 2018.

[5] J. D. Boles, J. J. Piel, and D. J. Perreault, "Enumeration and analysis of dc-dc converter implementations based on piezoelectric resonators," *IEEE Transactions on Power Electronics*, vol. 36, no. 1, pp. 129–145, 2021.

[6] B. Pollet, G. Despesse, and F. Costa, "A new non-isolated low power inductorless piezoelectric dc-dc converter," *IEEE Transactions on Power Electronics*, vol. 34, no. 11, pp. 11 002–11 013, 2019.

[7] M. Touhami, G. Despesse, and F. Costa, "A new topology of dc-dc converter based on piezoelectric resonator," in *2020 IEEE 21st Workshop on Control and Modeling for Power Electronics (COMPEL)*. IEEE, 2020, pp. 1–7.

[8] W. Braun, E. Stolt, L. Gu, J. J. Segovia-Fernandez, S. Chakraborty, R. Lu, and J. M. R. Davila, "Optimized resonators for piezoelectric power conversion," *IEEE Open Journal of Power Electronics*, 2021.

[9] M. Touhami, G. Despesse, F. Costa, and B. Pollet, "Implementation of control strategy for step-down DC-DC converter based on piezoelectric resonator," in *2020 22nd European Conference on Power Electronics and Applications (EPE'20 ECCE Europe)*. IEEE, 2020, pp. 1–9.

[10] S. Moon and J.-H. Park, "High power dc–dc conversion applications of disk-type radial mode Pb (Zr, Ti) O3 ceramic transducer," *Japanese Journal of Applied Physics*, vol. 50, no. 9S2, p. 09ND20, 2011.

[11] A. M. Flynn and S. R. Sanders, "Fundamental limits on energy transfer and circuit considerations for piezoelectric transformers," *IEEE Transactions on Power Electronics*, vol. 17, no. 1, pp. 8–14, 2002.

[12] J. M. Alonso, C. Ordiz, and M. A. Dalla Costa, "A novel control method for piezoelectric-transformer based power supplies assuring zero-voltage-switching operation," *IEEE Transactions on Industrial Electronics*, vol. 55, no. 3, pp. 1085–1089, 2008.

[13] M. Ekhtiari, T. Andersen, M. A. Andersen, and Z. Zhang, "Dynamic optimum dead time in piezoelectric transformer-based switch-mode power supplies," *IEEE Transactions on Power Electronics*, vol. 32, no. 1, pp. 783–793, 2017.

[14] E. L. Horsley, A. V. Carazo, N. Nguyen-Quang, M. P. Foster, and D. A. Stone, "Analysis of inductorless zero-voltage-switching piezoelectric transformer-based converters," *IEEE Transactions on Power Electronics*, vol. 27, no. 5, pp. 2471–2483, 2012.

[15] J. D. Boles, E. Ng, J. H. Lang, and D. J. Perreault, "High-efficiency operating modes for isolated piezoelectric-transformer-based dc-dc converters," in *Proc. IEEE Workshop on Control and Modeling for Power Electronics*, Aalborg, Denmark, Nov. 2020, pp. 1–8.

[16] E. Ng, J. D. Boles, J. H. Lang, and D. J. Perreault, "Non-isolated dc-dc converter implementations based on piezoelectric transformers," in *Proc. IEEE Energy Conversion Congress and Exposition*, Vancouver, Canada, Oct. 2021, pp. 1–8.

[17] Z. Yang, J. Forrester, J. N. Davidson, M. P. Foster, and D. A. Stone, "Resonant current estimation and phase-locked loop feedback design for piezoelectric transformer-based power supplies," *IEEE Transactions on Power Electronics*, vol. 35, no. 10, pp. 10 466–10 476, 2020.

[18] J. Forrester, J. N. Davidson, M. P. Foster, and D. A. Stone, "Influence of spurious modes on the efficiency of piezoelectric transformers: A sensitivity analysis," *IEEE Transactions on Power Electronics*, vol. 36, no. 1, pp. 617–629, 2020.

[19] A. Vazquez Carazo, "Piezoelectric transformers: An historical review," in *Actuators*, vol. 5, no. 2. MDPI, 2016, p. 12.

[20] S. Dong, A. V. Carazo, and S. H. Park, "Equivalent circuit and optimum design of a multilayer laminated piezoelectric transformer," *IEEE transactions on ultrasonics, ferroelectrics, and frequency control*, vol. 58, no. 12, pp. 2504–2515, 2011.

[21] M. Khanna, R. Burgos, Q. Wang, K. D. Ngo, and A. V. Carazo, "New tunable piezoelectric transformers and their application in dc–dc converters," *IEEE Transactions on Power Electronics*, vol. 32, no. 12, pp. 8974–8978, 2017.

[22] K. S. Meyer, M. A. Andersen, and F. Jensen, "Parameterized analysis of zero voltage switching in resonant converters for optimal electrode layout of piezoelectric transformers," in *2008 IEEE Power Electronics Specialists Conference*. IEEE, 2008, pp. 2543–2548.

[23] E. Horsley, M. Foster, and D. Stone, "State-of-the-art piezoelectric transformer technology," in *2007 European Conference on Power Electronics and Applications*. IEEE, 2007, pp. 1–10.

[24] A. M. Sánchez, M. Sanz, R. Prieto, J. A. Oliver, P. Alou, and J. A. Cobos, "Design of piezoelectric transformers for power converters by means of analytical and numerical methods," *IEEE transactions on industrial electronics*, vol. 55, no. 1, pp. 79–88, 2008.

[25] G. Ivensky, I. Zafrany, and S. Ben-Yaakov, "Generic operational characteristics of piezoelectric transformers," *IEEE Transactions on Power Electronics*, vol. 17, no. 6, pp. 1049–1057, 2002.

[26] Y.-P. Liu, D. Vasic, F. Costa, W.-J. Wu, and C.-K. Lee, "Design of fixed frequency controlled radial-mode stacked disk-type piezoelectric transformers for dc/dc converter applications," *Smart Materials and Structures*, vol. 18, no. 8, p. 085025, 2009.

[27] L. Wang and R. P. Burgos, "Comprehensive analysis of models and operational characteristics of piezoelectric transformers," in *Proc. IEEE Applied Power Electronics Conference and Exposition*, New Orleans, LA, USA, Mar. 2020, pp. 1422–1429.

[28] K. Uchino, "High-power piezoelectrics and loss mechanisms," in *Advanced Piezoelectric Materials*. Elsevier, 2017, pp. 647–754.

[29] J. Erhart, P. Půlpán, and M. Pustka, *Piezoelectric Ceramic Resonators*. Springer, 2017.

[30] H. H. Woodson and J. R. Melcher, *Electromechanical Dynamics Part III: Elastic and Fluid Media*. Wiley, 1968.

[31] K. S. Van Dyke, "The piezo-electric resonator and its equivalent network," *Proceedings of the Institute of Radio Engineers*, vol. 16, no. 6, pp. 742–764, 1928.

[32] A. Ballato, "Modeling piezoelectric and piezomagnetic devices and structures via equivalent networks," *IEEE Transactions on Ultrasonics, Ferroelectrics, and Frequency Control*, vol. 48, no. 5, pp. 1189–1240, 2001.

[33] S. Sherrit, S. P. Leary, B. P. Dolgin, and Y. Bar-Cohen, "Comparison of the Mason and KLM equivalent circuits for piezoelectric resonators in the thickness mode," in *Proc. IEEE Ultrasonics International Symposium*, vol. 2, Tahoe, NV, USA, Oct. 1999, pp. 921–926.

[34] K. Uchino and S. Hirose, "Loss mechanisms in piezoelectrics: how to measure different losses separately," *IEEE Transactions on Ultrasonics, ferroelectrics, and frequency control*, vol. 48, no. 1, pp. 307–321, 2001.

[35] "Physical and piezoelectric properties of APC materials". APC International, Ltd. [Online]. Available: https://www.americanpiezo.com/apc-materials/physical-piezoelectric-properties.html

[36] "Ceramic materials". Boston Piezo Optics Inc. [Online]. Available: https://www.bostonpiezooptics.com/ceramic-materials-pzt

[37] "Material properties". Piezo Technologies. [Online]. Available: https://piezotechnologies.com/materials-chart/

[38] "Physical and piezoelectric properties of t&p materials". T&Partners Praha. [Online]. Available: https://www.tpartnerspraha.com/maretials-type-1.html

[39] "Material data". PI Ceramic GmbH. [Online]. Available: https://static.piceramic.com/fileadmin/user_upload/physik_instrumente/files/datasheets/PI_Ceramic_Material_Data.pdf

[40] "PZT materials complete properties". CTS Corporation. [Online]. Available: https://www.ctscorp.com/wp-content/uploads/CTS_-PZT-Materials_Complete-Properties_20180829.pdf

[41] "Piezo ceramics". Fuji Ceramics Corporation. [Online]. Available: http://www.fujicera.co.jp/managed/wp-content/themes/fujicera/digitalbook/en/elements/index_h5.html#1

[42] "Piezoceramic hard materials material data". CeramTec. [Online]. Available: https://www.ceramtec.com/files/ms_piezoceramic-hard-materials_en_de.pdf

[43] "Material coefficients PIC181". PI Ceramic.

[44] "Lithium niobate". Boston Piezo Optics Inc. [Online]. Available: https://www.bostonpiezooptics.com/lithium-niobate

[45] "Ready to deliver piezoelectric ceramics". APC International. [Online]. Available: https://www.americanpiezo.com/piezo-sale/piezoelectric-ceramics.html

[46] D. Costinett, D. Maksimovic, and R. Zane, "Circuit-oriented treatment of nonlinear capacitances in switched-mode power supplies," *IEEE Transactions on Power Electronics*, vol. 30, no. 2, pp. 985–995, 2014.